An ALE approach for large-deformation thermoplasticity with application to friction welding

MMO Hamed[1] AT McBride[2] BD Reddy[1]

[1]Centre for Research in Computational Mechanics, University of Cape Town, 7701 Rondebosch, South Africa

[2]Glasgow Computational Engineering Centre, University of Glasgow, G12 8LT, UK

hmdmai001@myuct.ac.za, andrew.mcbride@glasgow.ac.uk, daya.reddy@uct.ac.za

Abstract

This work describes the development and implementation of a large-deformation solver with thermomechanical friction contact for numerical simulation in applications such as friction welding processes. A finite strain associative coupled thermoplasticity model is used: this resolves the viscoplastic deformations in the thermomechanically affected zone as well as the elastic stresses in the parent material. An arbitrary Lagrangian-Eulerian (ALE) formulation for coupled finite strain thermoplasticity is developed and incorporated into the solver, in which the motion of the reference configuration is represented incrementally through a reference velocity field. Thus, the deformation from the material configuration is required neither explicitly in terms of a deformation field, nor implicitly in terms of the deformation gradient. A range of benchmark examples serves to elucidate features of the model and computational procedure, also through comparison with a fully Lagrangian approach. Simulation of a direct drive friction welding problem illustrates the robustness and reliability of the new numerical approach.

1 Introduction

Computational simulations of complex manufacturing and related processes are now routinely adopted, often alongside experimental approaches, in the design and manufacture of components in an industrial context. The underlying models are generally highly coupled and nonlinear, and so represent non-trivial challenges in the development of robust and accurate computational

models and associated algorithms. A typical example, and one which motivates the work presented here, concerns friction welding, a family of solid-state joining processes where friction is used to generate the heat necessary for welding. Friction welds are formed in three stages: first, mechanical friction at the contact surface between the workpieces and the tool, if one is present, produces heat, raising the temperature around the interface. In the second stage, the combined effect of the elevated temperature and compressive and shear stresses plasticises the material in the vicinity of the friction region. In the third stage, the frictional force is removed and a forging force is maintained so that the plasticised material solidifies in the presence of compressive stress to form the weld. Modelling of such a process therefore requires taking account of material behaviour that would be modelled as thermoviscoplastic, with heat generation and transfer; and contact, which might be modelled as frictional or frictionless. In particular, it is essential to take proper account of the interaction between frictional contact forces and viscoplastic stresses in a thermomechanically affected zone. The family of friction welding processes includes friction stir welding (FSW) [32], linear friction welding (LFW)[21], and rotary friction welding (RFW) [8, 35].

Numerical simulation of friction stir welding has been the subject of much research: see for example the reviews [12, 24]. Computational approaches to LFW and RFW have also been the subject of numerical approaches, with some examples being the studies reported in [33, 9, 18, 19]. A literature review of strategies for numerical simulation of linear friction welding was presented in [6], while reviews of the literature on FSW and LFW are presented in [12, 6, 20].

Many of the early numerical approaches to RFW were based on CFD models. A coupled thermomechanical model of IFW was developed in [22], where the material was modelled by an incompressible temperature-dependent viscoplastic Norton–Hoff law. The model in [5] on the other hand was based on the Navier-Stokes equations with a non-Newtonian viscosity. A 3D rigid viscoplastic simulation of direct drive friction welding was carried out in [38], while numerical simulation of direct drive friction welding using a modified Carreau fluid constitutive model was reported in [26]. Other numerical work includes simulations of IFW and FHPP [10, 37, 15].

In processes such as friction welding the challenges in numerical simulation of the interaction between frictional contact forces and viscoplastic stresses stem from the large deformations in

the thermomechanically affected zone (TMAZ), as well as the large range of strain rate values. The extent of deformations in the TMAZ would result in excessive mesh distortions in the case of finite element-based simulations, which would necessitate frequent remeshing or the adoption of an Arbitrary Lagrangian Eulerian (ALE) formulation [12, 6].

The two main formulations of ALE for finite strain plasticity in the literature [25, 3] are not suited to addressing these challenges. First, they both rely on keeping track of the significant deformation from the initial material configuration, either explicitly by representing the initial material configuration as a variable, or implicitly by keeping track of the deformation gradient. Second, both formulations rely on a split step approach, which comprises a Lagrangian step where the deformed configuration is computed with the mesh velocity kept constant, and an Eulerian step where the mesh is updated keeping the deformation fixed. The large range of deformation rate values within the weld is such that updating the deformation in a Lagrangian step without excessive mesh distortion would require a very small time step, which may increase the required simulation time to prohibitive durations.

The aim of this work is to address these challenges by implementing a novel Arbitrary Lagrangian Eulerian (ALE) procedure for numerical simulation of thermomechanical processes involving viscoplastic materials undergoing large deformations, with thermomechanical frictional contact, in which the motion is represented in terms of an intermediate reference configuration by a combination of the deformation and the reference velocity. The deformation from the material configuration is required neither explicitly – through the material configuration field – nor implicitly by tracking the deformation gradient. Instead, the material configuration is referenced in terms of the reference velocity, so that excessive deformation in the TMAZ does not cause numerical difficulties. Also, the stresses are resolved by simultaneously updating the deformation and the reference velocity, so that the number of time steps required to simulate the weld remains reasonably small, preventing excessive computational expense. The finite strain plasticity and finite deformation thermomechanical frictional contact formulations are extended by including the contribution of the reference velocity. A Newton-Raphson procedure, with the use of consistent tangent moduli, is adopted, in this way ensuring the second-order convergence properties of the method.

The model is implemented in C++, leveraging deal.II [4], an object-oriented library that enables

rapid development of numerical simulation codes inter alia by providing classes that compute element degrees of freedom and element shape functions. The model is set up to run on distributed memory parallel computing systems.

The structure of the rest of this work is as follows. Section 2 is concerned with the relevant kinematics, including that required for the ALE formulation and for multibody frictional contact. Section 3 comprises an overview of the balance equations, and the constitutive relations for finite strain thermoviscoplasticity and for thermomechanical frictional contact. The weak formulation of the problem is developed in Section 4, and the time- and spatially discrete versions follow. Details of the predictor-corrector approach adopted for updating plastic behaviour are given here, as are details of the mechanical-thermal operator split proces and the ALE iteration procedure. In Section 5 a range of benchmark problems is presented so as to elucidate key features of the model and the computational procedure. The latter includes a comparison between the current ALE procedure with a fully Lagrangian approach. Then, in Section 6 the approach is applied to a friction welding problem. These examples illustrate the reliability and robustness of the new numerical approach. The work concludes with summarizing remarks and an indication of avenues for further work on this topic.

2 Kinematics, the ALE formulation, and contact

2.1 Configurations and fields of a deformable body

We consider two deformable bodies undergoing thermomechanical frictional contact. We designate one the contactor and the other the target and index them, respectively, by 'con' and 'tar', see Figure 1. They are denoted in the material configuration by $\Omega_0^{\mathcal{B}} \subset \mathbb{R}^3$, $\mathcal{B} \in \{\text{con}, \text{tar}\}$. The motion is defined by $\boldsymbol{x} = \boldsymbol{\varphi}_0(\boldsymbol{X}_0, t)$, which is invertible with respect to the first parameter and which maps the material configuration $\Omega_0^{\mathcal{B}}$ to the current configuration $\tilde{\Omega}^{\mathcal{B}} := \{\boldsymbol{x} = \boldsymbol{\varphi}_0(\boldsymbol{X}_0, t) | \boldsymbol{X}_0 \in \Omega_0^{\mathcal{B}}\}$. The local deformation state from the reference configuration is described by the deformation gradient $\boldsymbol{F} = \partial \boldsymbol{\varphi}_0 / \partial \boldsymbol{X}_0$. A field $q := q_0(\boldsymbol{X}_0, t)$ has the spatial form $q = \tilde{q}(\boldsymbol{x}, t) = q_0(\boldsymbol{\varphi}_0^{-1}(\boldsymbol{x}, t), t)$. The spatial and material gradients of q are denoted, respectively,

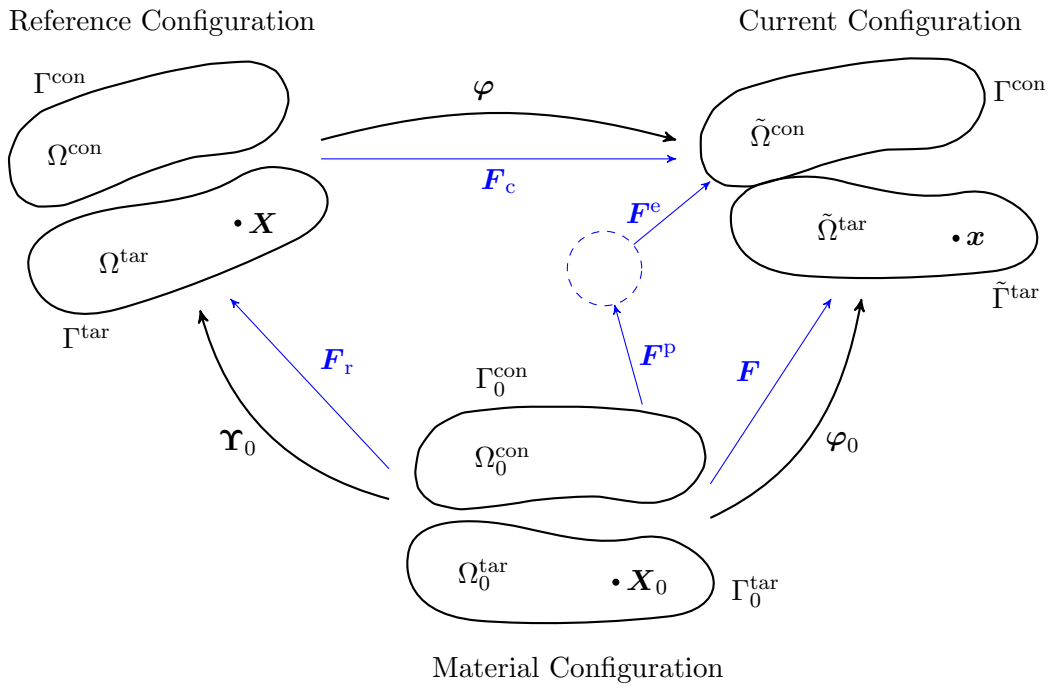

Figure 1: Configurations of contacting bodies

by

$$\nabla q \coloneqq \operatorname{grad} q \coloneqq \frac{\partial \tilde{q}}{\partial \boldsymbol{x}}\,, \qquad \text{and} \qquad \operatorname{Grad}_0 q \coloneqq \frac{\partial q_0}{\partial \boldsymbol{X}_0}. \tag{2.1}$$

The first and second partial time derivatives of the motion at a fixed material point are, respectively, the material velocity $\boldsymbol{v}$ and acceleration $\boldsymbol{a}$:

$$\boldsymbol{v} \coloneqq \dot{\boldsymbol{x}} \coloneqq \frac{\partial}{\partial t}\boldsymbol{\varphi}_0(\boldsymbol{X}_0, t)\,, \qquad \boldsymbol{a} \coloneqq \ddot{\boldsymbol{x}} \coloneqq \frac{\partial^2}{\partial t^2}\boldsymbol{\varphi}_0(\boldsymbol{X}_0, t)\,. \tag{2.2}$$

In general, we adopt the notations

$$\dot{q} \coloneqq \frac{\mathrm{D}q}{\mathrm{D}t} \coloneqq \frac{\partial q_0}{\partial t}\,. \tag{2.3}$$

Continuity and material impenetrability conditions require throughout the motion that the Jacobian determinant J of the deformation gradient satisfy $J \coloneqq \det(\boldsymbol{F}) > 0$.

In an Arbitrary Lagrangian Eulerian (ALE) configuration, fields are given as functions of position in an arbitrary reference configuration $\Omega^{\mathcal{B}}$ given by the reference motion $\boldsymbol{\Upsilon}_0 \colon \Omega_0^{\mathcal{B}} \times \mathbb{R}^+ \to \mathbb{R}^3$, which is continuous and invertible with respect to the first parameter, with $\Omega^{\mathcal{B}} \coloneqq \{\boldsymbol{X} = \boldsymbol{\Upsilon}_0(\boldsymbol{X}_0, t) | \boldsymbol{X}_0 \in \Omega_0^{\mathcal{B}}\}$.

A field $q = q_0(\boldsymbol{X}_0, t)$ is given in the reference configuration by $q = q(\boldsymbol{X}, t) = q_0(\boldsymbol{\Upsilon}_0^{-1}(\boldsymbol{X}, t), t)$. The gradient of a scalar field q and the gradient and divergence of a tensor field $\boldsymbol{q}$ in the reference configuration are denoted, respectively, by

$$\text{Grad } q \coloneqq \frac{\partial}{\partial \boldsymbol{X}} q(\boldsymbol{X}, t)\,, \quad \text{Grad } \boldsymbol{q} \coloneqq \frac{\partial}{\partial \boldsymbol{X}} \boldsymbol{q}(\boldsymbol{X}, t)\,, \quad \text{Div } \boldsymbol{q} \coloneqq (\text{Grad } \boldsymbol{q}) : \mathbf{1}.$$

In particular, the gradient of the motion $\boldsymbol{\varphi}$ in the reference configuration is denoted by

$$\boldsymbol{F}_{\mathrm{c}} \coloneqq \frac{\partial}{\partial \boldsymbol{X}} \boldsymbol{\varphi}(\boldsymbol{X}, t) = \frac{\partial}{\partial \boldsymbol{X}} \varphi_0(\boldsymbol{\Upsilon}_0^{-1}(\boldsymbol{X}, t), t)\,, \tag{2.4}$$

where the subscript c refers to the current configuration. It is related to the deformation gradient through the chain rule, by

$$\boldsymbol{F} = \boldsymbol{F}_{\mathrm{c}} \boldsymbol{F}_{\mathrm{r}}\,, \tag{2.5}$$

where $\boldsymbol{F}_{\mathrm{r}}$ is the reference motion gradient defined by $\boldsymbol{F}_{\mathrm{r}} \coloneqq \text{Grad}_0\, \boldsymbol{\Upsilon}_0$.

Gradients in the reference and current configurations are related, through the chain rule, by

$$\frac{\partial\, \tilde{\bullet}}{\partial \boldsymbol{x}} = \frac{\partial\, \bullet}{\partial \boldsymbol{X}} \left(\frac{\partial \boldsymbol{x}}{\partial \boldsymbol{X}} \right)^{-1}\,; \tag{2.6}$$

that is,

$$\nabla \bullet = (\text{Grad } \bullet)\, \boldsymbol{F}_{\mathrm{c}}^{-1}\,. \tag{2.7}$$

The material time derivative of the reference motion is the reference velocity

$$\boldsymbol{V} \coloneqq \frac{\partial}{\partial t} \boldsymbol{\Upsilon}_0(\boldsymbol{X}_0, t). \tag{2.8}$$

It gives the material time derivative in the reference configuration of a field $q(\boldsymbol{X}, t)$ as

$$\dot{q}(\boldsymbol{X}, t) = \left(\frac{\partial q}{\partial t} + (\text{Grad } q) \cdot \boldsymbol{V} \right) \Big|_{(\boldsymbol{X}, t)}\,. \tag{2.9}$$

The velocity is then given in the reference configuration by

$$\boldsymbol{v} = \frac{\partial \boldsymbol{\varphi}}{\partial t} + \boldsymbol{F}_{\mathrm{c}} \boldsymbol{V}\,. \tag{2.10}$$

Similarly, the acceleration is given by

$$\boldsymbol{a} = \frac{\partial^2 \boldsymbol{\varphi}}{\partial t^2} + 2\left(\frac{\partial \boldsymbol{F}_{\mathrm{c}}}{\partial t}\right)\boldsymbol{V} + \boldsymbol{F}_{\mathrm{c}}\left(\frac{\partial \boldsymbol{V}}{\partial t} + (\mathrm{Grad}\ \boldsymbol{V})\,\boldsymbol{V}\right) + ((\mathrm{Grad}\ \boldsymbol{F}_{\mathrm{c}})\,\boldsymbol{V})\,\boldsymbol{V}\,. \tag{2.11}$$

The velocity gradient in the reference configuration is defined by

$$\boldsymbol{L} \coloneqq \mathrm{Grad}\,\boldsymbol{V} = \dot{\boldsymbol{F}}_{\mathrm{r}}\boldsymbol{F}_{\mathrm{r}}^{-1}\,. \tag{2.12}$$

Its symmetric and skew symmetric parts are, respectively, $\boldsymbol{D} = \frac{1}{2}\left(\boldsymbol{L} + \boldsymbol{L}^{\mathrm{t}}\right)$, and $\boldsymbol{W} = \frac{1}{2}\left(\boldsymbol{L} - \boldsymbol{L}^{\mathrm{t}}\right)$.

2.1.1 Material remapping operator

Let $\square$ be any scalar or tensor field given as a function of position in the reference configuration and time as $\square = \square(\boldsymbol{X}, t)$ and as a function of position in the material configuration and time as $\square = \square_0(\boldsymbol{X}_0, t)$. Then, for a point $\boldsymbol{X}$ in the reference configuration, and two time instants t, $\tau > 0$, we define the material remapping operator $\mathcal{M}$ by

$$\mathcal{M}_\tau^t\{\square\}\big|_{\boldsymbol{X}} \coloneqq \mathcal{M}(\square, \boldsymbol{X}, \tau, t) \coloneqq \square_0\left(\boldsymbol{\Upsilon}_0^{-1}(\boldsymbol{X}, t), \tau\right)\,. \tag{2.13}$$

The operator $\mathcal{M}$ remaps the material configuration such that any point $\boldsymbol{X}_0$ is identified by its position $\boldsymbol{X}$ in the reference configuration at time t: $\boldsymbol{X} = \boldsymbol{\Upsilon}_0(\boldsymbol{X}_0, t)$. Position in the reference configuration is itself a valid input to the operator $\mathcal{M}$, since it is given as a function of position in the reference configuration and time by the identity function, and is given as a function of position in the material configuration and time by the reference motion $\boldsymbol{\Upsilon}_0$. Thus,

$$\mathcal{M}_\tau^t\{\boldsymbol{X}\} = \boldsymbol{\Upsilon}_0\left(\boldsymbol{\Upsilon}_0^{-1}(\boldsymbol{X}, t), \tau\right)\,. \tag{2.14}$$

Since $\square(\boldsymbol{X}, \tau) = \square_0(\boldsymbol{\Upsilon}_0^{-1}(\boldsymbol{X}, \tau), \tau)$, we get

$$\begin{aligned}\square(\mathcal{M}_\tau^t\{\boldsymbol{X}\}, \tau) &= \square_0(\boldsymbol{\Upsilon}_0^{-1}(\mathcal{M}_\tau^t\{\boldsymbol{X}\}, \tau), \tau)\\ &= \square_0(\boldsymbol{\Upsilon}_0^{-1}(\boldsymbol{\Upsilon}_0\left(\boldsymbol{\Upsilon}_0^{-1}(\boldsymbol{X}, t), \tau\right), \tau), \tau) = \square_0\left(\boldsymbol{\Upsilon}_0^{-1}(\boldsymbol{X}, t), \tau\right)\,,\end{aligned} \tag{2.15}$$

which, by definition (2.13), gives

$$\mathcal{M}_\tau^t\{\square\}\big|_{\boldsymbol{X}} = \square\left(\mathcal{M}_\tau^t\{\boldsymbol{X}\}, \tau\right)\,. \tag{2.16}$$

This obviates the requirement of keeping track of the material configuration for evaluating $\mathcal{M}_\tau^t\{\square\}\big|_{\boldsymbol{X}}$, as long as $\mathcal{M}_\tau^t\{\boldsymbol{X}\}$ is known, which is the position in the reference configuration at time τ of the material point whose position in the reference configuration at time t is $\boldsymbol{X}$.

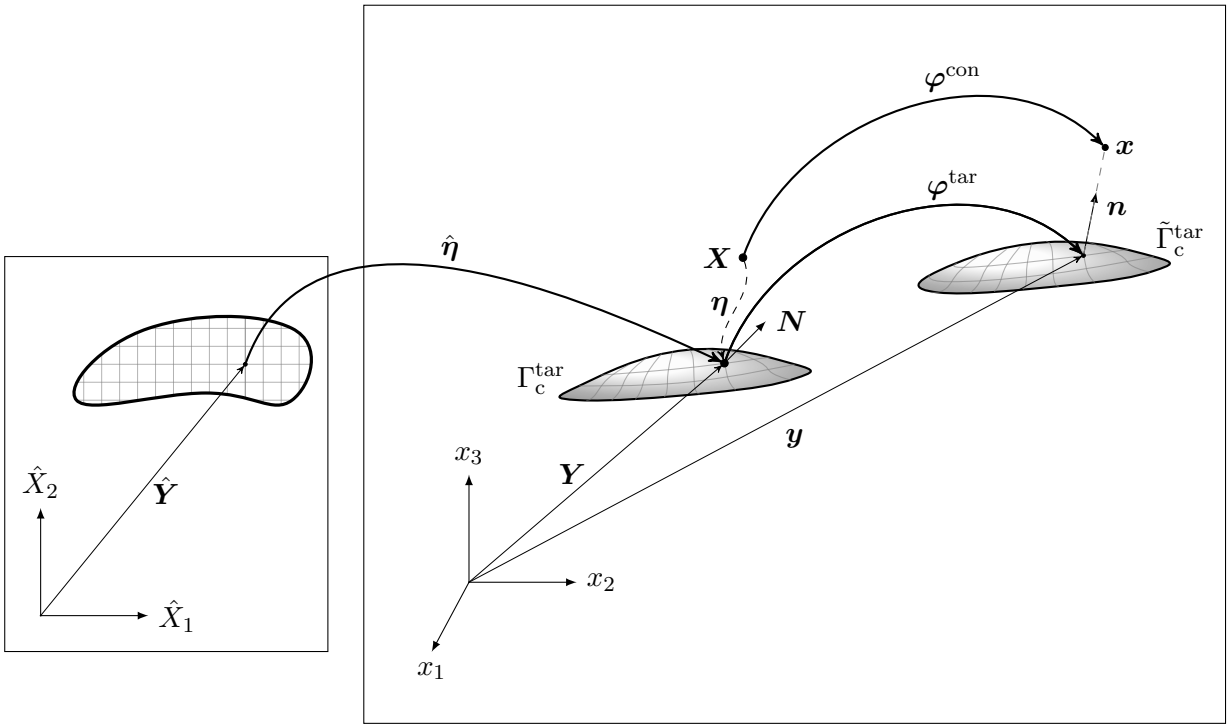

Figure 2: Contact target surface configurations

2.2 Multibody frictional contact

Frictional contact occurs between two deformable bodies, a contactor and a target, which are given in the reference configuration, respectively, by Ω^{con} and $\Omega^{\mathrm{tar}} \subset \mathbb{R}^3$. The subset of the boundary of each body that may potentially come into contact with the other is denoted, in the reference configuration, by $\Gamma_{\mathrm{c}}^{\mathcal{B}} \subseteq \partial\Omega^{\mathcal{B}}$, $\mathcal{B} \in \{\mathrm{con}, \mathrm{tar}\}$.

The target surface in the reference configuration $\Gamma_{\mathrm{c}}^{\mathrm{tar}} \subset \mathbb{R}^3$ is parameterised by a region $\hat{\Gamma}^{\mathrm{tar}} \subset \mathbb{R}^2$ through a continuous bijective mapping $\hat{\boldsymbol{\eta}} : \hat{\Gamma}^{\mathrm{tar}} \to \Gamma_{\mathrm{c}}^{\mathrm{tar}}$ such that $\boldsymbol{Y} = \hat{\boldsymbol{\eta}}(\hat{\boldsymbol{Y}})$. For each contactor point $\boldsymbol{X} \in \Gamma_{\mathrm{c}}^{\mathrm{con}}$, a corresponding target point $\boldsymbol{Y} = \boldsymbol{\eta}(\boldsymbol{X}, t) \in \Gamma_{\mathrm{c}}^{\mathrm{tar}}$ is considered such that the distance in the current configuration is minimized between the two points $\boldsymbol{x} = \boldsymbol{\varphi}(\boldsymbol{X}, t)$ and $\boldsymbol{y} = \boldsymbol{\varphi}(\boldsymbol{Y}, t)$. Thus, the contactor point $\boldsymbol{X}$ is related to $\hat{\boldsymbol{Y}}$ by $\hat{\boldsymbol{Y}} = \hat{\boldsymbol{Y}}(\boldsymbol{X}, t) \coloneqq \hat{\boldsymbol{\eta}}^{-1}(\boldsymbol{\eta}(\boldsymbol{X}, t)) \in \hat{\Gamma}^{\mathrm{tar}}$, and for any $\hat{\boldsymbol{Y}}' \in \hat{\Gamma}^{\mathrm{tar}}$, by

$$\left\| \boldsymbol{\varphi}^{\mathrm{con}}(\boldsymbol{X}, t) - \boldsymbol{\varphi}^{\mathrm{tar}}\left(\hat{\boldsymbol{\eta}}\left(\hat{\boldsymbol{Y}}(\boldsymbol{X}, t)\right), t\right) \right\| = \min_{\hat{\boldsymbol{Y}}'} \left\| \boldsymbol{\varphi}^{\mathrm{con}}(\boldsymbol{X}, t) - \boldsymbol{\varphi}^{\mathrm{tar}}\left(\hat{\boldsymbol{\eta}}\left(\hat{\boldsymbol{Y}}'\right), t\right) \right\|, \tag{2.17}$$

which implies

$$\left[\boldsymbol{\varphi}^{\mathrm{con}}(\boldsymbol{X},t)-\boldsymbol{\varphi}^{\mathrm{tar}}\left(\boldsymbol{\eta}(\boldsymbol{X},t),t\right)\right]\cdot\left\{\left[\frac{\partial}{\partial\boldsymbol{Y}}\bigg|_{\boldsymbol{Y}=\boldsymbol{\eta}(\boldsymbol{X},t)}\boldsymbol{\varphi}^{\mathrm{tar}}(\boldsymbol{Y},t)\right]\frac{\partial\hat{\boldsymbol{\eta}}}{\partial\hat{\boldsymbol{Y}}}\bigg|_{\hat{\boldsymbol{Y}}=\hat{\boldsymbol{Y}}(\boldsymbol{X},t)}\right\}=\boldsymbol{0}\,. \tag{2.18}$$

The contact geometry is represented in Figure 2.

The partial time derivative of the position $\boldsymbol{y}=\boldsymbol{\varphi}^{\mathrm{tar}}\left(\boldsymbol{\eta}\left(\boldsymbol{X},t\right),t\right)$ of the target point in the current configuration is given by

$$\frac{\partial}{\partial t}\varphi_i^{\mathrm{tar}}(\boldsymbol{\eta}(\boldsymbol{X},t),t)=\frac{\partial}{\partial t}\varphi_i^{\mathrm{tar}}(\boldsymbol{Y},t)\bigg|_{\boldsymbol{Y}=\boldsymbol{\eta}(\boldsymbol{X},t)}+\left[\frac{\partial}{\partial Y_j}\varphi_i^{\mathrm{tar}}\left(\boldsymbol{Y},t\right)\bigg|_{\boldsymbol{Y}=\boldsymbol{\eta}(\boldsymbol{X},t)}\right]\frac{\partial}{\partial t}\eta_j(\boldsymbol{X},t)\,. \tag{2.19}$$

We denote the gradients with respect to $\hat{\boldsymbol{Y}}$ of the target position in the reference and current configurations, respectively, by

$$\boldsymbol{\Xi}=\boldsymbol{\Xi}(\hat{\boldsymbol{Y}})\coloneqq\frac{\partial\hat{\boldsymbol{\eta}}}{\partial\hat{\boldsymbol{Y}}}\,, \tag{2.20}$$

$$\boldsymbol{G}=\boldsymbol{G}(\boldsymbol{Y},t)\coloneqq\left[\frac{\partial}{\partial\boldsymbol{Y}}\boldsymbol{\varphi}^{\mathrm{tar}}(\boldsymbol{Y},t)\right]\frac{\partial\hat{\boldsymbol{\eta}}}{\partial\hat{\boldsymbol{Y}}}\bigg|_{\hat{\boldsymbol{Y}}=\hat{\boldsymbol{\eta}}^{-1}(\boldsymbol{Y})}\,. \tag{2.21}$$

Then equation (2.18) becomes

$$\left[\boldsymbol{\varphi}^{\mathrm{con}}(\boldsymbol{X},t)-\boldsymbol{\varphi}^{\mathrm{tar}}\left(\boldsymbol{\eta}(\boldsymbol{X},t),t\right)\right]\cdot\boldsymbol{G}\left(\boldsymbol{\eta}(\boldsymbol{X},t),t\right)=\boldsymbol{0}\,. \tag{2.22}$$

For a fixed contactor point $\boldsymbol{X}\in\Gamma_{\mathrm{c}}^{\mathrm{con}}$ and a target point $\boldsymbol{Y}=\boldsymbol{\eta}(\boldsymbol{X},t)\in\Gamma_{\mathrm{c}}^{\mathrm{tar}}$, the partial time derivative of $\boldsymbol{G}(\boldsymbol{\eta}(\boldsymbol{X},t),t)$ is, using the chain rule,

$$\begin{aligned}\frac{\partial}{\partial t}G_{ij}\left(\boldsymbol{\eta}(\boldsymbol{X},t),t\right)=&\left(\frac{\partial}{\partial t}\left[\varphi_{i,k}\left(\boldsymbol{Y},t\right)\right]\bigg|_{\boldsymbol{Y}=\boldsymbol{\eta}(\boldsymbol{X},t)}\right)\Xi_{kj}\left(\hat{\boldsymbol{Y}}(\boldsymbol{X},t)\right)\\&+\left(\frac{\partial}{\partial\hat{Y}_l}\left[G_{ij}\left(\hat{\boldsymbol{\eta}}(\hat{\boldsymbol{Y}}),t\right)\right]\bigg|_{\hat{\boldsymbol{Y}}=\hat{\boldsymbol{Y}}(\boldsymbol{X},t)}\right)\frac{\partial}{\partial t}\hat{Y}_l\left(\boldsymbol{X},t\right)\,,\end{aligned} \tag{2.23}$$

where

$$\begin{aligned}\frac{\partial}{\partial\hat{Y}_l}G_{ij}\left(\hat{\boldsymbol{\eta}}(\hat{\boldsymbol{Y}}),t\right)=&\varphi_{i,km}\left(\hat{\boldsymbol{\eta}}(\hat{\boldsymbol{Y}}),t\right)\Xi_{ml}\left(\hat{\boldsymbol{Y}}\right)\Xi_{kj}\left(\hat{\boldsymbol{Y}}\right)\\&+\varphi_{i,k}\left(\hat{\boldsymbol{\eta}}(\hat{\boldsymbol{Y}}),t\right)\;\hat{\eta}_{k,jl}\left(\hat{\boldsymbol{Y}}\right)\,.\end{aligned} \tag{2.24}$$

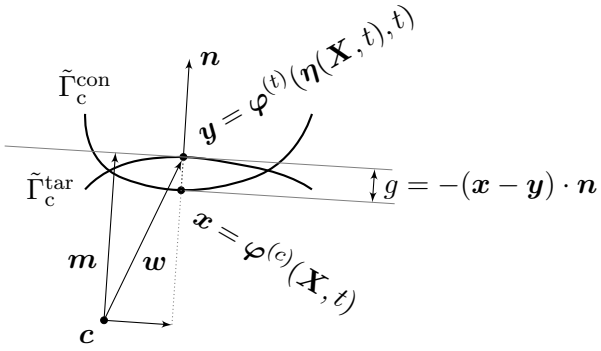

Figure 3: Normal contact penetration

Similarly, the partial time derivative of $\boldsymbol{\eta}\left(\boldsymbol{X},t\right)=\hat{\boldsymbol{\eta}}\left(\hat{\boldsymbol{Y}}(\boldsymbol{X},t)\right)$ is

$$\begin{aligned}\frac{\partial}{\partial t}\boldsymbol{\eta}(\boldsymbol{X},t) &= \left(\frac{\partial}{\partial\hat{\boldsymbol{Y}}}\hat{\boldsymbol{\eta}}(\hat{\boldsymbol{Y}})\Big|_{\hat{\boldsymbol{Y}}=\hat{\boldsymbol{Y}}(\boldsymbol{X},t)}\right)\frac{\partial}{\partial t}\hat{\boldsymbol{Y}}(\boldsymbol{X},t)\\ &= \boldsymbol{\Xi}\left(\hat{\boldsymbol{Y}}(\boldsymbol{X},t)\right)\frac{\partial}{\partial t}\hat{\boldsymbol{Y}}(\boldsymbol{X},t)\,.\end{aligned}\tag{2.25}$$

In turn, the partial time derivative of $\hat{\boldsymbol{Y}}(\boldsymbol{X},t)$ is obtained by differentiating both sides of (2.22)and making use of (2.23) to get

$$\frac{\partial}{\partial t}\hat{Y}_k\left(\boldsymbol{X},t\right)=\left[\mathcal{A}_{jk}\left(\boldsymbol{X},t\right)\right]^{-1}\mathcal{V}_j\left(\boldsymbol{X},t\right)\,,\tag{2.26}$$

where

$$\begin{aligned}\mathcal{A}_{jk}\left(\boldsymbol{X},t\right) &= G_{ij}(\boldsymbol{\eta}(\boldsymbol{X},t),t)\,G_{ik}(\boldsymbol{\eta}(\boldsymbol{X},t),t)\\ &\quad-\left[\varphi_i^{\mathrm{con}}(\boldsymbol{X},t)-\varphi_i^{\mathrm{tar}}(\boldsymbol{\eta}(\boldsymbol{X},t),t)\right]\frac{\partial}{\partial\hat{Y}_k}\left[G_{ij}\left(\hat{\boldsymbol{\eta}}(\hat{\boldsymbol{Y}}),t\right)\right]\Big|_{\hat{\boldsymbol{Y}}=\hat{\boldsymbol{Y}}(\boldsymbol{X},t)}\,,\end{aligned}\tag{2.27}$$

and

$$\begin{aligned}\mathcal{V}_j\left(\boldsymbol{X},t\right) &= \left[\varphi_i^{\mathrm{con}}(\boldsymbol{X},t)-\varphi_i^{\mathrm{tar}}(\boldsymbol{\eta}(\boldsymbol{X},t),t)\right]\left(\frac{\partial}{\partial t}\left[\varphi_{i,k}^{\mathrm{tar}}\left(\boldsymbol{Y},t\right)\right]\Big|_{\boldsymbol{Y}=\boldsymbol{\eta}(\boldsymbol{X},t)}\right)\Xi_{kj}\left(\hat{\boldsymbol{Y}}(\boldsymbol{X},t)\right)\\ &\quad+\left[\frac{\partial}{\partial t}\varphi_i^{\mathrm{con}}(\boldsymbol{X},t)-\frac{\partial}{\partial t}\varphi_i^{\mathrm{tar}}(\boldsymbol{Y},t)\Big|_{\boldsymbol{Y}=\boldsymbol{\eta}(\boldsymbol{X},t)}\right]G_{ij}(\boldsymbol{\eta}(\boldsymbol{X},t),t)\,.\end{aligned}\tag{2.28}$$

Normal contact. The penetration g is defined by (Figure 3)

$$g(\boldsymbol{X},t)\coloneqq-\left[\boldsymbol{\varphi}^{\mathrm{con}}(\boldsymbol{X},t)-\boldsymbol{\varphi}^{\mathrm{tar}}(\boldsymbol{\eta}(\boldsymbol{X},t),t)\right]\cdot\boldsymbol{n}\left(\boldsymbol{\eta}(\boldsymbol{X},t),t\right)\leq 0\,,\tag{2.29}$$

where $\boldsymbol{n} = \boldsymbol{n}(\boldsymbol{Y}, t)$ is the outward unit normal of the target surface in the current configuration $\boldsymbol{\varphi}^{\mathrm{tar}}(\Gamma_{\mathrm{c}}^{\mathrm{tar}}, t)$ at $\boldsymbol{y} = \boldsymbol{\varphi}^{\mathrm{tar}}(\boldsymbol{Y}, t)$ with $\boldsymbol{Y} = \boldsymbol{\eta}(\boldsymbol{X}, t) \in \Gamma_{\mathrm{c}}^{\mathrm{tar}}$.

The partial time derivative of the unit normal

$$\frac{\partial \boldsymbol{n}}{\partial t} = -\left(\boldsymbol{G}\left(\boldsymbol{G}^{\mathrm{t}}\boldsymbol{G}\right)^{-1}\frac{\partial \boldsymbol{G}^{\mathrm{t}}}{\partial t}\right)\boldsymbol{n}\,. \tag{2.30}$$

Slip velocity. The contact slip velocity, which is defined as the projection of the difference between the contactor and target velocities onto the plane tangent to the target surface, is

$$\begin{aligned}
\boldsymbol{v}_s &\coloneqq \boldsymbol{G}\left(\boldsymbol{G}^{\mathrm{t}}\boldsymbol{G}\right)^{-1}\boldsymbol{G}^{\mathrm{t}}\left(\boldsymbol{v}^{\mathrm{con}} - \boldsymbol{v}^{\mathrm{tar}}\right)\,,\\
&= \boldsymbol{G}\left(\boldsymbol{G}^{\mathrm{t}}\boldsymbol{G}\right)^{-1}\boldsymbol{G}^{\mathrm{t}}\left(\frac{\partial \boldsymbol{\varphi}^{\mathrm{con}}}{\partial t} - \left.\frac{\partial \boldsymbol{\varphi}^{\mathrm{tar}}}{\partial t}\right|_{\boldsymbol{Y}=\boldsymbol{\eta}(\boldsymbol{X},t)}\right)\\
&\quad + \boldsymbol{G}\left(\boldsymbol{G}^{\mathrm{t}}\boldsymbol{G}\right)^{-1}\boldsymbol{G}^{\mathrm{t}}\left(\left(\mathrm{Grad}\,\boldsymbol{\varphi}^{\mathrm{con}}\right)\boldsymbol{V}^{\mathrm{con}} - \left(\mathrm{Grad}\,\boldsymbol{\varphi}^{\mathrm{tar}}\right)\boldsymbol{V}^{\mathrm{tar}}\right)\,,
\end{aligned} \tag{2.31}$$

using (2.10). The use of equation (2.30) with

$$G_{ij}\frac{\partial \hat{Y}_j}{\partial t} = \varphi_{i,k}\Xi_{kj}\frac{\partial \hat{Y}_j}{\partial t} = \varphi_{i,j}\frac{\partial \eta_j}{\partial t}\,, \tag{2.32}$$

$$\left(\varphi_m^{\mathrm{con}} - \varphi_m^{\mathrm{tar}}\right) = -g n_m\,, \tag{2.33}$$

and substitution in (2.31) gives the slip velocity

$$\boldsymbol{v}_s = \left(\mathrm{Grad}\,\boldsymbol{\varphi}^{\mathrm{tar}}\right)\frac{\partial \boldsymbol{\eta}}{\partial t} - g\frac{\partial \boldsymbol{n}}{\partial t} + \boldsymbol{G}\left(\boldsymbol{G}^{\mathrm{t}}\boldsymbol{G}\right)^{-1}\boldsymbol{G}^{\mathrm{t}}\left(\left(\mathrm{Grad}\,\boldsymbol{\varphi}^{\mathrm{con}}\right)\boldsymbol{V}^{\mathrm{con}} - \left(\mathrm{Grad}\,\boldsymbol{\varphi}^{\mathrm{tar}}\right)\boldsymbol{V}^{\mathrm{tar}}\right)\,. \tag{2.34}$$

3 Governing equations and constitutive models

3.1 Governing balance equations

Balance of momentum. We denote by $\boldsymbol{\sigma}$ the symmetric Cauchy stress tensor, and by $\boldsymbol{P}$ the first Piola-Kirchhoff stress which is related to $\boldsymbol{\sigma}$ by

$$\boldsymbol{P} = J\boldsymbol{\sigma}\boldsymbol{F}^{-t}\,. \tag{3.1}$$

We will also require the Kirchhoff stress

$$\boldsymbol{\tau} = J\boldsymbol{\sigma}\,. \tag{3.2}$$

With these definitions the equation of balance of linear momentum is, in the current configuration,

$$\rho\frac{D\boldsymbol{v}}{Dt} - \operatorname{div}\boldsymbol{\sigma} = \rho\boldsymbol{f}\,. \tag{3.3}$$

The corresponding equation in the reference configuration is

$$\rho_m\frac{D\boldsymbol{v}}{Dt} - \operatorname{Div}\boldsymbol{P} = \boldsymbol{f}_b\,, \tag{3.4}$$

where $\boldsymbol{f}_b$ is the external force per unit volume in the reference configuration and ρ_{m} is the mass density per unit volume in the reference configuration.

Mechanical boundary conditions. Boundary conditions corresponding to the momentum equation are as follows:

$$\boldsymbol{\varphi}(\boldsymbol{X},t) = \boldsymbol{\varphi}_{\mathrm{pre}}(\boldsymbol{X},t) \qquad \text{on } \Gamma^{\mathcal{B}}_{D_\mu} \subset \Gamma^{\mathcal{B}}\,, \tag{3.5a}$$

$$\boldsymbol{V}(\boldsymbol{X},t) = \boldsymbol{V}_{\mathrm{pre}}(\boldsymbol{X},t) \qquad \text{on } \Gamma^{\mathcal{B}}_{V} \subset \Gamma^{\mathcal{B}}\,, \tag{3.5b}$$

$$\boldsymbol{\sigma}\,\boldsymbol{n} = \boldsymbol{f}_s \qquad \text{on } \Gamma^{\mathcal{B}}_{N_\mu} \subset \Gamma^{\mathcal{B}}\,. \tag{3.5c}$$

Here, $\Gamma^{\mathcal{B}}_{D_\mu}$ is the subset of $\Gamma^{\mathcal{B}}$ where an essential boundary condition is given on the deformation, $\Gamma^{\mathcal{B}}_{V}$ is the subset where an essential boundary condition on the velocity is given, and $\Gamma^{\mathcal{B}}_{N_\mu}$ is that where a natural boundary condition on the boundary traction is given.

Furthermore, on each contact boundary pair $\Gamma_{\mathrm{c}}^{\mathrm{con}}$ and $\Gamma_{\mathrm{c}}^{\mathrm{tar}}$, contact boundary conditions are given by

$$\boldsymbol{\sigma}^{\mathrm{con}}\boldsymbol{n}^{\mathrm{con}} = \boldsymbol{f}_{\mathrm{c}} \qquad \text{on } \Gamma_{\mathrm{c}}^{\mathrm{con}}\,, \tag{3.6a}$$

$$\boldsymbol{\sigma}^{\mathrm{tar}}\boldsymbol{n}^{\mathrm{tar}} = -\boldsymbol{f}_{\mathrm{c}} \qquad \text{on } \Gamma_{\mathrm{c}}^{\mathrm{tar}} \tag{3.6b}$$

where $\boldsymbol{f}_{\mathrm{c}}$ is the contact force.

Initial conditions. At time t_0, the initial deformation and reference velocity are prescribed:

$$\boldsymbol{\varphi}(\boldsymbol{X},t_0) = \boldsymbol{x}_{\mathrm{initial}}(\boldsymbol{X})\,, \tag{3.7a}$$

$$\boldsymbol{V}(\boldsymbol{X},t_0) = \boldsymbol{V}_{\mathrm{initial}}(\boldsymbol{X})\,. \tag{3.7b}$$

Balance of energy. The local form of balance of energy is [29]

$$-J \operatorname{div}\left[\frac{1}{J}\boldsymbol{q}\right] + \mathcal{R}_b = \dot{e} - \boldsymbol{\tau} : \boldsymbol{d}\,, \tag{3.8}$$

where $\mathcal{R}_b$ is the heat source per unit volume in the reference configuration and e is the internal energy.

3.2 Finite strain thermoplasticity

An appropriate model for plastic behaviour is the coupled thermomechanical J_2-flow theory for associative thermoplasticity at finite strains [29]. The model is based on a multiplicative decomposition of the deformation gradient into its elastic and plastic parts; that is,

$$\boldsymbol{F} = \boldsymbol{F}^e \boldsymbol{F}^p\,. \tag{3.9}$$

We define in addition the elastic left and plastic right Cauchy-Green deformation tensors respectively by

$$\boldsymbol{b}^e = \boldsymbol{F}^e \boldsymbol{F}^{e^t}\,, \quad \boldsymbol{C}^p = \boldsymbol{F}^{p^t} \boldsymbol{F}^p\,, \quad \boldsymbol{G}^p = (\boldsymbol{C}^p)^{-1}\,. \tag{3.10}$$

Plastic deformation is assumed volume preserving, so that $\det \boldsymbol{F}^p = 1$. As a consequence, the Jacobian is equal to that for the elastic part of the deformation gradient: that is, $J = \det \boldsymbol{F} = \det \boldsymbol{F}^e$.

One may decompose $\boldsymbol{b}^e$ into a volume-preserving part $\bar{\boldsymbol{b}}^e$ and a volumetric part J according to

$$\boldsymbol{b}^e = J^{2/3} \bar{\boldsymbol{b}}^e\,, \quad \det \bar{\boldsymbol{b}}^e = 1\,. \tag{3.11}$$

The total time derivative of $\boldsymbol{b}^e$ is given by

$$\begin{aligned} \dot{\boldsymbol{b}}^e &= \dot{\boldsymbol{F}} \boldsymbol{G}^p \boldsymbol{F}^{\mathrm{t}} + \boldsymbol{F} \boldsymbol{G}^p \dot{\boldsymbol{F}}^{\mathrm{t}} + \boldsymbol{F} \dot{\boldsymbol{G}}^p \boldsymbol{F}^{\mathrm{t}} \\ &= \boldsymbol{l} \boldsymbol{b}^e + \boldsymbol{b}^e \boldsymbol{l}^{\mathrm{t}} + \mathscr{L}_v \boldsymbol{b}^{\mathrm{e}}, \end{aligned} \tag{3.12}$$

where

$$\mathscr{L}_v \boldsymbol{b}^{\mathrm{e}} \coloneqq \boldsymbol{F} \dot{\boldsymbol{G}}^{\mathrm{p}} \boldsymbol{F}^{\mathrm{t}} \tag{3.13}$$

is the Lie derivative of $\boldsymbol{b}^e$.

Multiplicative split in the reference configuration. We start by defining

$$\boldsymbol{B}^e := \boldsymbol{F}_{\rm r}\boldsymbol{G}^p\boldsymbol{F}_{\rm r}^{\rm t}\,, \tag{3.14}$$

so that $\boldsymbol{b}^e$ can be expressed in the form

$$\boldsymbol{b}^e = \boldsymbol{F}_{\rm c}\boldsymbol{B}^e\boldsymbol{F}_{\rm c}^{\rm t}\,. \tag{3.15}$$

Then, the elastic strain rate (3.12) can be written as

$$\dot{\boldsymbol{b}}^{\rm e} = \dot{\boldsymbol{F}}_{\rm c}\boldsymbol{B}^{\rm e}\boldsymbol{F}_{\rm c}^{\rm t} + \boldsymbol{F}_{\rm c}\boldsymbol{B}^{\rm e}\dot{\boldsymbol{F}}_{\rm c}^{\rm t} + \boldsymbol{F}_{\rm c}\left[\boldsymbol{L}\boldsymbol{B}^{\rm e} + \boldsymbol{B}^{\rm e}\boldsymbol{L}^{\rm t}\right]\boldsymbol{F}_{\rm c}^{\rm t} + \mathscr{L}_v\boldsymbol{b}^{\rm e} \tag{3.16}$$

$$= \left[\dot{\boldsymbol{F}}_{\rm c}\boldsymbol{F}_{\rm c}^{-1} + \boldsymbol{F}_{\rm c}\boldsymbol{L}\boldsymbol{F}_{\rm c}^{-1}\right]\boldsymbol{b}^{\rm e} + \boldsymbol{b}^{\rm e}\left[\dot{\boldsymbol{F}}_{\rm c}\boldsymbol{F}_{\rm c}^{-1} + \boldsymbol{F}_{\rm c}\boldsymbol{L}\boldsymbol{F}_{\rm c}^{-1}\right]^{\rm t} + \mathscr{L}_v\boldsymbol{b}^{\rm e}\,. \tag{3.17}$$

Balance of energy. For thermoplastic bodies the total entropy η is assumed to be additively decomposable into elastic and plastic parts [29] so that

$$\eta = \eta^e + \eta^p\,. \tag{3.18}$$

The internal energy, introduced in (3.8), is then related to the free energy ψ through $\psi = e - \eta^e\theta$. Elastic and thermal behaviour are defined through a free energy function

$$\psi = \hat{\psi}\left(J, \bar{\boldsymbol{b}}^e, \theta, \alpha\right)\,. \tag{3.19}$$

We define the dissipation

$$\mathcal{D} := \theta\dot{\eta} + \boldsymbol{\tau} : \boldsymbol{d} - \dot{e} \geq 0\,. \tag{3.20}$$

Application of the now-standard Coleman-Noll procedure to (3.20), using also (3.19), gives

$$\boldsymbol{\tau} = 2\frac{\partial\hat{\psi}}{\partial\boldsymbol{b}^e}\boldsymbol{b}^e, \quad \eta^e = -\frac{\partial\hat{\psi}}{\partial\theta}, \quad \beta = -\frac{\partial\hat{\psi}}{\partial\alpha}\,. \tag{3.21}$$

The use of these expressions in the dissipation then leads to the expression

$$\mathcal{D} := \underbrace{\boldsymbol{\tau} : [-\tfrac{1}{2}(\mathcal{L}_v\boldsymbol{b}^e)(\boldsymbol{b}^e)^{-1} + \beta\dot{\alpha}}_{\mathcal{D}_{\rm mech}} + \underbrace{\theta\dot{\eta}^p}_{\mathcal{D}_{\rm therm}}\,, \tag{3.22}$$

in which the mechanical and thermal contributions $\mathcal{D}_{\rm mech}$ and $\mathcal{D}_{\rm therm}$ are also made explicit. The equation of balance of energy can then be written in the form

$$-J\,\mathrm{div}\left[\frac{1}{J}\boldsymbol{q}\right] + \mathcal{R}_b = \theta\dot{\eta}^e - \mathcal{D}_{\rm mech}\,. \tag{3.23}$$

Furthermore the evolution equation for the temperature becomes [29]

$$c\dot{\theta} = (\mathcal{D}_{\text{mech}} - \mathcal{H}) + \left[\mathcal{R}_b - \text{Div}\left(\boldsymbol{F}_{\text{c}}^{-1}\boldsymbol{q}\right)\right] , \tag{3.24}$$

in which the structural heating $\mathcal{H}$ is defined by

$$\mathcal{H} = -\theta\frac{\partial}{\partial\theta}\left(\boldsymbol{\tau}\colon\boldsymbol{d} - \mathcal{D}_{\text{mech}}\right) , \tag{3.25}$$

and the specific heat capacity c per unit volume in the reference configuration is given by

$$c = -\theta\frac{\partial^2\hat{\psi}}{\partial\theta^2} .$$

Thermal boundary conditions. The thermal boundary conditions are

$$\theta(\boldsymbol{X},t) = \bar{\theta}(\boldsymbol{X},t) \qquad \text{on } \Gamma^{\mathcal{B}}_{D_\theta} \subset \Gamma^{\mathcal{B}} , \tag{3.26a}$$

$$\boldsymbol{q}\cdot\ \boldsymbol{n} = \mathcal{R}_s \qquad \text{on } \Gamma^{\mathcal{B}}_{N_\theta} \subset \Gamma^{\mathcal{B}} , \tag{3.26b}$$

where $\Gamma^{\mathcal{B}}_{D_\theta}$ and $\Gamma^{\mathcal{B}}_{N_\theta}$ are complementary subsets of $\Gamma^{\mathcal{B}}$ such that $\Gamma^{\mathcal{B}}_{D_\theta} \cap \Gamma^{\mathcal{B}}_{N_\theta} = \emptyset$. In addition, on each contact boundary pair $\Gamma^{\text{con}}_{\text{c}}$ and $\Gamma^{\text{tar}}_{\text{c}}$, thermal contact boundary conditions are given in terms of the contact heat flux q_{hc} and the frictional heat generation $\mathcal{D}^{\mathcal{B}}_{\text{fric}}$ by

$$\boldsymbol{q}^{\text{con}}\cdot\boldsymbol{n}^{\text{con}} = \mathcal{D}^{\text{con}}_{\text{fric}} + q_{\text{hc}} \qquad \text{on } \Gamma^{\text{tar}}_{\text{c}} , \tag{3.27a}$$

$$\boldsymbol{q}^{\text{tar}}\cdot\boldsymbol{n}^{\text{tar}} = \mathcal{D}^{\text{tar}}_{\text{fric}} - q_{\text{hc}} \qquad \text{on } \Gamma^{\text{tar}}_{\text{c}} . \tag{3.27b}$$

The thermal initial condition is given by

$$\theta(\boldsymbol{X},t_0) = \theta_{\text{initial}}(\boldsymbol{X}) . \tag{3.28}$$

The free energy function. We adopt a free energy function of the form [29]

$$\hat{\psi} = \hat{T}(\theta) + \hat{M}(J,\theta) + \hat{U}(J) + \hat{W}(\bar{\boldsymbol{b}}^e) + \hat{K}(\alpha), \tag{3.29}$$

with

$$\hat{U}(J) = \kappa\left[\frac{1}{2}\left(J^2-1\right) - \ln J\right] \quad \text{and} \quad \hat{W}(\bar{\boldsymbol{b}}^e) = \int\frac{\mu}{2}\left(\log\bar{\boldsymbol{b}}^{\text{e}}\right)\left(\bar{\boldsymbol{b}}^{\text{e}}\right)^{-1}\colon \text{d}\bar{\boldsymbol{b}}^{\text{e}} , \tag{3.30}$$

and where μ and κ are the elastic shear and bulk moduli.

From $(3.21)_1$ and taking account of the volumetric-deviatoric split, the Kirchhoff stress tensor $\boldsymbol{\tau} = J\boldsymbol{\sigma}$ is then given by

$$\boldsymbol{\tau} = J\left(\frac{\partial\hat{\psi}}{\partial J}\right)\mathbf{1} + 2\frac{\partial\hat{\psi}}{\partial\bar{\boldsymbol{b}}^e}\bar{\boldsymbol{b}}^e, \tag{3.31}$$

so that the elastic relation is given in terms of the deviatoric and spherical parts of the stress, respectively $\operatorname{dev}\boldsymbol{\tau}$ and p, by

$$\operatorname{dev}\boldsymbol{\tau} = \mu \log \bar{\boldsymbol{b}}^{\mathrm{e}}\,, \tag{3.32a}$$

$$p = \kappa\left(J^2 - 1\right)\,. \tag{3.32b}$$

The yield criterion and flow relation[29]. The yield function is defined by

$$\phi = \hat{\phi}(\boldsymbol{\tau}, \beta, \theta), \tag{3.33}$$

The flow relations corresponding to associative plasticity with a normality law are then

$$\mathscr{L}_v \boldsymbol{b}^e = -2\gamma[\partial_{\boldsymbol{\tau}}\hat{\phi}]\boldsymbol{b}^e\,, \quad \dot{\alpha} = \gamma\partial_\beta\hat{\phi}\,, \quad \dot{\eta}^{\mathrm{p}} = \gamma\partial_\theta\hat{\phi}\,, \tag{3.34}$$

where η^p as before is the plastic entropy, together with the complementarity conditions

$$\phi \le 0, \quad \gamma \ge 0, \quad \gamma\phi = 0\,, \tag{3.35}$$

where γ is a non-negative scalar multiplier.

Viscoplastic behaviour. We extend the plasticity model to accommodate viscoplastic behaviour, by prescribing the viscoplastic yield stress $\sigma^y = \sigma^y(\alpha, \dot{\alpha}, \theta)$, together with the von Mises yield criterion:

$$\phi = |\operatorname{dev}\boldsymbol{\tau}|\,\sqrt{\tfrac{2}{3}}\sigma^y(\alpha, \dot{\alpha}, \theta) \le 0\,. \tag{3.36}$$

One of the most commonly used among these constitutive models is the Johnson-Cook model [13], which has been used in several works on simulation of FSW [27, 11, 34]:

$$\sigma^y = [A + B(\alpha)^n]\left[1 + C\ln\left(\frac{\dot{\alpha}}{\dot{\varepsilon}_0^{vp}}\right)\right]\left[1 - \left(\frac{\theta - \theta_{\mathrm{R}}}{\theta_{\mathrm{M}} - \theta_{\mathrm{R}}}\right)^m\right]\,. \tag{3.37}$$

Here A, B, C, m and n are model parameters, θ_{R} and θ_{M} are respectively the reference and melting temperatures, and $\dot{\varepsilon}_0^{vp}$ is the reference strain rate.

A further form for the yield stress that will also be used in computations is that adapted from the constitutive law described in [26]. Specifically, the constitutive law is modified so that strain rate dependence only takes effect when the strain rate exceeds a temperature-dependent minimum value $\dot{\varepsilon}_{\min}$ given by

$$\dot{\varepsilon}_{\min} = \left(1 - \left(\frac{\theta - \theta_{\mathrm{R}}}{\theta_{\mathrm{M}} - \theta_{\mathrm{R}}}\right)^m\right)\dot{\varepsilon}_0\,. \tag{3.38}$$

The strain rate value used in the constitutive law is then taken to be the greater of the two values: the equivalent plastic strain rate $\dot{\alpha}$ and this minimum value $\dot{\varepsilon}_{\min}$:

$$\dot{\varepsilon} = \max(\dot{\alpha}, \dot{\varepsilon}_{\min})\,. \tag{3.39}$$

The flow stress is then given as a function of a strain-rate independent yield strength $\sigma_{\mathrm{s}}^{\mathrm{y}}$ and the modified strain rate $\dot{\varepsilon}$ as

$$\sigma^{\mathrm{y}} = 3\left\{\left[1+\left(\left(\frac{\sigma_{\mathrm{s}}^{\mathrm{y}}}{3\dot{\varepsilon}_0\mu_0}\right)^{\frac{1}{d-1}}\frac{\dot{\varepsilon}}{\dot{\varepsilon}_0}\right)^2\right]^{\frac{d-1}{2}}(\mu_0-\mu_\infty)+\mu_\infty\right\}\dot{\varepsilon}\,, \tag{3.40}$$

$$\sigma_{\mathrm{s}}^{\mathrm{y}} = (A+B\alpha^n)\left(1-\left(\frac{\theta-\theta_{\mathrm{R}}}{\theta_{\mathrm{M}}-\theta_{\mathrm{R}}}\right)^m\right)\,. \tag{3.41}$$

Finally, the expressions for the mechanical dissipation, structural heating and heat flux are

$$\mathcal{D}_{\mathrm{mech}} = \sqrt{\tfrac{2}{3}}\gamma\sigma^y, \qquad \mathcal{H} = -\theta\dot{J}\frac{\partial^2\hat{\psi}}{\partial\theta\partial J}, \qquad \boldsymbol{q} = -k\ \mathrm{grad}\ \theta, \tag{3.42}$$

where k is the thermal conductivity in Fourier's heat conduction law.

3.3 Thermomechanical frictional contact

Mechanical contact. The contact conditions are concisely expressed as the complementarity conditions

$$g \le 0 \quad f_N \ge 0\,, \quad f_N \cdot g = 0\,, \tag{3.43}$$

in which g is the gap (see (2.29)), and $f_N \coloneqq -\boldsymbol{n}\cdot\boldsymbol{f}_{\mathrm{c}}$ is the normal traction. The stick-slip condition of the tangential contact tractions is given in terms of the tangential component of the contact traction $\boldsymbol{f}_T \coloneqq \boldsymbol{f}_{\mathrm{c}} - (\boldsymbol{n}\cdot\boldsymbol{f}_{\mathrm{c}})\,\boldsymbol{n}$, the stick limit $\Phi\left(\boldsymbol{f}_T, f_N\right)$, and a Lagrange multiplier ν, by the complementarity conditions [30]

$$\Phi\left(\boldsymbol{f}_T, f_N\right) \le 0\,, \quad \nu \ge 0\,, \quad \nu\Phi = 0\,, \tag{3.44}$$

and the evolution law

$$\boldsymbol{v}_s = \nu\frac{\partial\Phi}{\partial\boldsymbol{f}_T}\,, \tag{3.45}$$

where the slip velocity $\boldsymbol{v}_s$, given by (2.34), is the tangential component of the relative velocity between the contactor and the target in the current configuration.

Thermal contact. The heat flux through the contact interface is given by [1]

$$q_{\mathrm{hc}} = \hat{h}(t_N, \theta_G) g_\theta(\boldsymbol{X}, t) \tag{3.46}$$

where $g_\theta(\boldsymbol{X}, t) \coloneqq \theta^{\mathrm{con}}(\boldsymbol{X}, t) - \theta^{\mathrm{tar}}(\boldsymbol{\eta}(\boldsymbol{X}, t), t)$ is the temperature difference across the interface. The heat transfer coefficient $\hat{h}$ is a function of the normal contact force t_N and the mean gas temperature, which is given in terms of the relative thermal effusivities $h_\epsilon^{\mathcal{B}}$, $i \in \{\mathrm{c}, \mathrm{t}\}$, and the temperatures at the contact interface by

$$\theta_G(\boldsymbol{X}, t) = h_\epsilon^{\mathrm{con}} \theta^{\mathrm{con}}(\boldsymbol{X}, t) + h_\epsilon^{\mathrm{tar}} \theta^{\mathrm{tar}}(\boldsymbol{\eta}(\boldsymbol{X}, t), t)\,. \tag{3.47}$$

Frictional heat generation due to tangential slip against frictional forces is modelled as a boundary heat source given by

$$\mathcal{D}_{\mathrm{fric}}^{\mathcal{B}} = h_\epsilon^{\mathcal{B}} \boldsymbol{v}_s \cdot \boldsymbol{f}_T\,, \quad i \in \{\mathrm{c}, \mathrm{t}\}\,. \tag{3.48}$$

4 Weak continuous and discrete formulations

4.1 Weak formulations

We take the inner product of equation (3.4) with an arbitrary test function $\delta\boldsymbol{u}$ that is sufficiently smooth and which satisfies the homogeneous form of the essential boundary conditions (3.5a) and (3.5b), and integrate over the reference configuration $\Omega^{\mathcal{B}}$. This gives

$$\int_{\Omega^{\mathcal{B}}} \delta\boldsymbol{u} \cdot \operatorname{Div} \boldsymbol{P}\, \mathrm{d}\Omega + \int_{\Omega^{\mathcal{B}}} \delta\boldsymbol{u} \cdot \boldsymbol{f}_b\, \mathrm{d}\Omega = \int_{\Omega^{\mathcal{B}}} \delta\boldsymbol{u} \cdot \rho_{\mathrm{m}} \boldsymbol{a}\, \mathrm{d}\Omega\,. \tag{4.1}$$

Integration by parts and use of the identity

$$\begin{aligned} \operatorname{Grad} \delta\boldsymbol{u} \colon \boldsymbol{\tau} \boldsymbol{F}_{\mathrm{c}}^{-\mathrm{t}} &= (\operatorname{Grad} \delta\boldsymbol{u})\, \boldsymbol{F}_{\mathrm{c}}^{-1} \colon \boldsymbol{\tau} \\ &= \nabla \delta\boldsymbol{u} \colon \boldsymbol{\tau}\,, \end{aligned} \tag{4.2}$$

gives the equation in the form

$$\int_{\Omega^{\mathcal{B}}} \delta\boldsymbol{u} \cdot \operatorname{Div} \boldsymbol{P} \, \mathrm{d}\Omega = -\int_{\Omega^{\mathcal{B}}} \nabla\delta\boldsymbol{u} \colon \boldsymbol{\tau} \, \mathrm{d}\Omega + \int_{\Gamma^{\mathcal{B}}_{N_\mu}} \delta\boldsymbol{u} \cdot \boldsymbol{f}_s \, J_\Gamma \, \mathrm{d}\Gamma + \int_{\Gamma^{\mathcal{B}}_{\mathrm{c}}} s^{\mathcal{B}} \delta\boldsymbol{u} \cdot \boldsymbol{f}_{\mathrm{c}} \, J_\Gamma \, \mathrm{d}\Gamma \,, \tag{4.3}$$

where we have used $J_\Gamma \coloneqq \mathrm{d}\tilde{\Gamma}/\mathrm{d}\Gamma = J\|\boldsymbol{F}^{-\mathrm{t}}\boldsymbol{N}\|$ and also substituted the surface forces from the boundary conditions (3.5c) and (3.6). The contact surface sign function $s^{\mathcal{B}}$, $\mathcal{B} \in \{\mathrm{con}, \mathrm{tar}\}$ is defined as

$$s^{\mathrm{con}} \coloneqq 1 \,, \;\; s^{\mathrm{tar}} \coloneqq -1 \,. \tag{4.4}$$

By substitution of (4.3) and following the convention of integrating the contribution of the target surface on the contactor surface instead [16], equation (4.1) becomes

$$\begin{aligned} \int_{\Omega^{\mathcal{B}}} \nabla\delta\boldsymbol{u} \colon \boldsymbol{\tau} \, \mathrm{d}\Omega + \int_{\Omega^{\mathcal{B}}} \delta\boldsymbol{u} \cdot \rho_{\mathrm{m}} \boldsymbol{a} \, \mathrm{d}\Omega - \int_{\Omega^{\mathcal{B}}} \delta\boldsymbol{u} \cdot \boldsymbol{f}_b \, \mathrm{d}\Omega \\ - \int_{\Gamma^{\mathcal{B}}_{N_\mu}} \delta\boldsymbol{u} \cdot \boldsymbol{f}_s \, J_\Gamma \, \mathrm{d}\Gamma - \int_{\Gamma^{\mathrm{con}}_{\mathrm{c}}} s^{\mathcal{B}} \delta\boldsymbol{u} \cdot \boldsymbol{f}_{\mathrm{c}} \, J_\Gamma \, \mathrm{d}\Gamma = 0 \,. \end{aligned} \tag{4.5}$$

The inertial force term can be expanded by substitution of equation (2.11) to obtain

$$\begin{aligned} \int_{\Omega^{\mathcal{B}}} \delta\boldsymbol{u} \cdot \rho_{\mathrm{m}} \boldsymbol{a} \, \mathrm{d}\Omega = \int_{\Omega^{\mathcal{B}}} \delta\boldsymbol{u} \cdot \rho_{\mathrm{m}} \Bigg[\frac{\partial^2 \boldsymbol{\varphi}}{\partial t^2} + 2 \left(\frac{\partial \boldsymbol{F}_{\mathrm{c}}}{\partial t} \right) \boldsymbol{V} + \boldsymbol{F}_{\mathrm{c}} \left(\frac{\partial \boldsymbol{V}}{\partial t} + (\operatorname{Grad} \boldsymbol{V}) \, \boldsymbol{V} \right) \\ + \left((\operatorname{Grad} \boldsymbol{F}_{\mathrm{c}}) \, \boldsymbol{V} \right) \boldsymbol{V} \Bigg] \, \mathrm{d}\Omega \,. \end{aligned} \tag{4.6}$$

The term involving $\operatorname{Grad} \boldsymbol{F}_{\mathrm{c}}$ can be simplified using integration by parts, to give eventually

$$\begin{aligned} \int_{\Omega^{\mathcal{B}}} \delta\boldsymbol{u} \cdot \rho_{\mathrm{m}} \boldsymbol{a} \, \mathrm{d}\Omega = \int_{\Omega^{\mathcal{B}}} \delta\boldsymbol{u} \cdot \rho_{\mathrm{m}} \left[\frac{\partial^2 \boldsymbol{\varphi}}{\partial t^2} + 2 \left(\frac{\partial \boldsymbol{F}_{\mathrm{c}}}{\partial t} \right) \boldsymbol{V} + \boldsymbol{F}_{\mathrm{c}} \left(\frac{\partial \boldsymbol{V}}{\partial t} \right) \right] \, \mathrm{d}\Omega \\ - \int_{\Omega^{\mathcal{B}}} \delta\boldsymbol{u} \cdot \operatorname{Div}(\rho_{\mathrm{m}} \boldsymbol{V}) \boldsymbol{F}_{\mathrm{c}} \boldsymbol{V} \, \mathrm{d}\Omega - \int_{\Omega^{\mathcal{B}}} \left((\operatorname{Grad} \, \delta\boldsymbol{u}) \, \boldsymbol{V} \right) \cdot \rho_{\mathrm{m}} \left(\boldsymbol{F}_{\mathrm{c}} \boldsymbol{V} \right) \, \mathrm{d}\Omega \\ + \int_{\Gamma^{\mathcal{B}}} \delta\boldsymbol{u} \cdot \rho_{\mathrm{m}} \left(\boldsymbol{F}_{\mathrm{c}} \boldsymbol{V} \right) \left(\boldsymbol{V} \cdot \boldsymbol{N} \right) \, \mathrm{d}\Gamma \,. \end{aligned} \tag{4.7}$$

For the thermal balance equation, the weak formulation is derived similarly by first multiplying equation (3.24) by an arbitrary test function $\delta\vartheta$ that is sufficiently smooth and which satisfies the homogeneous form of the essential boundary conditions (3.26a). Integration over the reference configuration $\Omega^{\mathcal{B}}$ gives

$$\int_{\Omega^{\mathcal{B}}} \delta\vartheta \; c\dot{\theta} \, \mathrm{d}\Omega = \int_{\Omega^{\mathcal{B}}} \delta\vartheta \; \left(\mathcal{D}_{\mathrm{mech}} - \mathcal{H} \right) \, \mathrm{d}\Omega + \int_{\Omega^{\mathcal{B}}} \delta\vartheta \; \left(\mathcal{R}_b - \operatorname{Div} \left(\boldsymbol{F}_{\mathrm{c}}^{-1} \boldsymbol{q} \right) \right) \, \mathrm{d}\Omega \,. \tag{4.8}$$

Integration by parts with the use of the chain rule, substitution of the boundary conditions 3.26b and 3.27, the use of 4.4 and finally substitution into (4.8) give

$$\int_{\Omega^{\mathcal{B}}} \nabla\delta\vartheta \cdot \boldsymbol{q}\, \mathrm{d}\Omega + \int_{\Omega^{\mathcal{B}}} \delta\vartheta\, c\dot{\theta}\, \mathrm{d}\Omega - \int_{\Omega^{\mathcal{B}}} \delta\vartheta\, (\mathcal{R}_b + \mathcal{D}_{\mathrm{mech}} - \mathcal{H})\, \mathrm{d}\Omega \\ - \int_{\Gamma^{\mathcal{B}}_{N_\theta}} \delta\vartheta\, \mathcal{R}_s\, \frac{J_\Gamma}{J}\, \mathrm{d}\Gamma - \int_{\Gamma_{\mathrm{c}}^{\mathrm{con}}} \delta\vartheta\, \left(\mathcal{D}^{\mathcal{B}}_{\mathrm{fric}} + s^{\mathcal{B}} q_{\mathrm{hc}}\right)\, \frac{J_\Gamma}{J}\, \mathrm{d}\Gamma = 0\,. \tag{4.9}$$

The problem statement is as follows:

Problem 4.1. *Find the deformation $\boldsymbol{\varphi}$, the reference velocity $\boldsymbol{V}$, and the temperature θ, in functional spaces defined on $\Omega^{\mathcal{B}} \times \mathbb{R}^+$, $i \in \{\mathrm{con}, \mathrm{tar}\}$ which satisfy the weak forms (4.5) and (4.9), and the essential boundary conditions (3.5a), (3.5b) and (3.26a) and initial conditions (3.7) and (3.28).*

The stress $\boldsymbol{\tau}$ is given by (3.32) and satisfies the yield criterion (3.36), where the elastic left Cauchy-Green deformation tensor $\boldsymbol{b}^{\mathrm{e}}$ evolves according to (3.34). The normal and tangential components of the contact force $\boldsymbol{f}_{\mathrm{c}}$ in (4.5) are given by (3.43) and 3.3), and the specific heat capacity c, the mechanical dissipation $\mathcal{D}_{mech}$, the structural heating $\mathcal{H}$, and the heat flux $\boldsymbol{q}$ are given by (3.2)

4.2 The discrete problem

4.2.1 Time discretization

First, time is discretized into N time steps $1, ..., N$, with each time step n corresponding to a time interval $[t_{n-1}, t_n]$. Temporal derivatives are approximated by finite differences given in terms of the time increment $\Delta t = t_n - t_{n-1}$ and of the values at t_n and t_{n-1}. The coupled thermomechanical problem corresponding to each time step is then approximated by a sequence of three smaller problems: a mechanical one, followed by a thermal one, and finally another mechanical problem.

Denoting the motion from the reference configuration, and its first and second partial time derivatives, by

$$\boldsymbol{\varphi}_n \coloneqq \boldsymbol{\varphi}|_{t=t_n}\,, \quad \left(\frac{\partial \boldsymbol{\varphi}}{\partial t}\right)_n \coloneqq \left(\frac{\partial \boldsymbol{\varphi}}{\partial t}\right)\Big|_{t=t_n}\,, \quad \left(\frac{\partial^2 \boldsymbol{\varphi}}{\partial t^2}\right)_n \coloneqq \left(\frac{\partial^2 \boldsymbol{\varphi}}{\partial t^2}\right)\Big|_{t=t_n}\,, \tag{4.10}$$

the updated first and second partial time derivatives at time step t_{n+1} are approximated using the updated motion $\boldsymbol{\varphi}_{n+1}$ through Newmark's method by

$$\left(\frac{\partial^2\boldsymbol{\varphi}}{\partial t^2}\right)_{n+1} = \frac{1}{\beta\Delta t^2}\left[\boldsymbol{\varphi}_{n+1} - \boldsymbol{\varphi}_n - \Delta t\left(\frac{\partial\boldsymbol{\varphi}}{\partial t}\right)_n\right] - \left(\frac{1}{2\beta} - 1\right)\left(\frac{\partial^2\boldsymbol{\varphi}}{\partial t^2}\right)_n , \tag{4.11a}$$

$$\left(\frac{\partial\boldsymbol{\varphi}}{\partial t}\right)_{n+1} = \left(\frac{\partial\boldsymbol{\varphi}}{\partial t}\right)_n + \Delta t\left[(1-\gamma)\left(\frac{\partial^2\boldsymbol{\varphi}}{\partial t^2}\right)_n + \gamma\left(\frac{\partial^2\boldsymbol{\varphi}}{\partial t^2}\right)_{n+1}\right] , \tag{4.11b}$$

where the Newmark parameters β and γ are computed using the generalized-α method [7]:

$$\gamma = \frac{1}{2} - \alpha_{\mathrm{m}} + \alpha_{\mathrm{f}} , \quad \beta = \frac{1}{4}(1 - \alpha_{\mathrm{m}} + \alpha_{\mathrm{f}})^2 , \tag{4.12}$$

$$\alpha_{\mathrm{m}} = \frac{2\rho_\infty - 1}{\rho_\infty + 1} , \quad \alpha_{\mathrm{f}} = \frac{\rho_\infty}{\rho_\infty + 1} , \quad \rho_\infty \in [0,1] . \tag{4.13}$$

The partial time derivative of the reference velocity $\partial\boldsymbol{V}/\partial t$ is approximated in a similar fashion to those of the motion (4.11). With the reference velocity $\boldsymbol{V}$ and its partial time derivative known at time $t = t_n$, the updated partial time derivative for a given updated reference velocity $\boldsymbol{V}_{n+1}$ is approximated by

$$\left(\frac{\partial\boldsymbol{V}}{\partial t}\right)_{n+1} = \frac{1}{\gamma\Delta t}\left(\boldsymbol{V}_{n+1} - \boldsymbol{V}_n\right) - \frac{1-\gamma}{\gamma}\left(\frac{\partial\boldsymbol{V}}{\partial t}\right)_n . \tag{4.14}$$

The thermal field is treated similarly. For a known temperature at time t_n $\theta_n \approx \theta|_{t=t_n}$, the updated partial time derivative of the temperature is approximated by the backward difference

$$\left(\frac{\partial\theta}{\partial t}\right)_{n+1} = \frac{1}{\Delta t}\left(\theta_{n+1} - \theta_n\right) . \tag{4.15}$$

The generalized midpoints α_{m} and α_{f} are used to define the generalized intermediate values $\bullet_{n+1-\alpha_{\mathrm{m}}}$ and $\bullet_{n+1-\alpha_{\mathrm{f}}}$ as

$$\bullet_{n+1-\alpha} = (1-\alpha)\left(\bullet_n\right) + \alpha\left(\bullet_{n+1}\right) , \quad \bullet_{n+1-\alpha} = (1-\alpha)\left(\bullet_n\right) + \alpha\left(\bullet_{n+1}\right) , \quad \alpha = \alpha_{\mathrm{f}} \text{ or } \alpha_{\mathrm{m}} . \tag{4.16}$$

Stress update. The stress $\boldsymbol{\tau}_{n+1}$ is given in terms of the deformation Jacobian J_{n+1} and the volume preserving part $\bar{\boldsymbol{b}}^{\mathrm{e}}_{n+1}$ of the elastic left Cauchy-Green tensor by (3.29) and (3.31) as

$$\boldsymbol{\tau}_{n+1} = \operatorname{dev}\boldsymbol{\tau}_{n+1} + p_{n+1}\mathbf{1} , \tag{4.17}$$

$$p_{n+1} = J_{n+1}\left\{\partial_J\left[\hat{M}(J_{n+1},\theta_{n+1}) + \hat{U}(J_{n+1})\right]\right\} , \tag{4.18}$$

$$\operatorname{dev}\boldsymbol{\tau}_{n+1} = 2\operatorname{dev}\left\{\left[\partial_{\bar{\boldsymbol{b}}^{\mathrm{e}}}\hat{W}(\bar{\boldsymbol{b}}^{\mathrm{e}}_{n+1})\right]\bar{\boldsymbol{b}}^{\mathrm{e}}_{n+1}\right\} , \tag{4.19}$$

where the deformation Jacobian is given in terms of the gradient of the motion in the reference configuration and the reference motion Jacobian by

$$J_{n+1} = \det\left[\mathrm{Grad}\,\boldsymbol{\varphi}_{n+1}\right] J_{\mathrm{r},n+1}\,. \tag{4.20}$$

The elastic left Cauchy-Green tensor $\boldsymbol{b}^{\mathrm{e}}_{n+1} = J^{2/3}_{n+1}\bar{\boldsymbol{b}}^{\mathrm{e}}_{n+1}$ and its volume-preserving part are given by

$$\boldsymbol{b}^{\mathrm{e}}_{n+1} = \boldsymbol{F}_{n+1}\boldsymbol{G}^{\mathrm{p}}_{n+1}\boldsymbol{F}^{\mathrm{t}}_{n+1}\,, \quad \bar{\boldsymbol{b}}^{\mathrm{e}}_{n+1} = J^{-2/3}_{n+1}\,\boldsymbol{b}^{\mathrm{e}}_{n+1}\,. \tag{4.21}$$

The material time derivative of the plastic tensor $\boldsymbol{G}^{\mathrm{p}}_{n+1}$ is given by (3.13) as

$$\dot{\boldsymbol{G}}^{\mathrm{p}}_{n+1} = \boldsymbol{F}^{-1}_{n+1}\mathscr{L}_v\boldsymbol{b}^{\mathrm{e}}_{n+1}\boldsymbol{F}^{-\mathrm{t}}_{n+1}\,, \tag{4.22}$$

where the Lie derivative $\mathscr{L}_v\boldsymbol{b}^{\mathrm{e}}_{n+1}$ is defined in (3.34) and evaluated at time t_{n+1}. Here, the consistency parameter γ_{n+1} is governed by the KKT conditions (3.35): and the time derivative of the equivalent plastic strain is

$$\dot{\alpha}_{n+1} = \sqrt{\tfrac{2}{3}}\gamma_{n+1}\,. \tag{4.23}$$

From (3.34) and (3.36),

$$\mathscr{L}_v\boldsymbol{b}^{\mathrm{e}}_{n+1} = -2\gamma_{n+1}\frac{\mathrm{dev}\,\boldsymbol{\tau}_{n+1}}{\|\mathrm{dev}\,\boldsymbol{\tau}_{n+1}\|}\boldsymbol{b}^{\mathrm{e}}_{n+1}\,. \tag{4.24}$$

A return mapping approach is used: this comprises a predictor step followed, if necessary, by a corrector step. In the predictor step, a trial solution is computed with $\gamma^{\mathrm{trial}}_{n+1}$: thus

$$\mathscr{L}_v\boldsymbol{b}^{\mathrm{e,trial}}_{n+1} = \boldsymbol{0}\,, \quad \alpha^{\mathrm{trial}}_{n+1} = \alpha_n\,, \quad \phi^{\mathrm{trial}}_{n+1} \coloneqq \left\|\mathrm{dev}\,\boldsymbol{\tau}^{\mathrm{trial}}_{n+1}\right\| - \sqrt{\tfrac{2}{3}}\sigma^{\mathrm{y}}(\alpha_n, 0, \theta_{n+1})\,. \tag{4.25}$$

Here, the trial stress deviator $\mathrm{dev}\,\boldsymbol{\tau}^{\mathrm{trial}}_{n+1}$ is computed using the trial left Cauchy-Green elastic tensor $\boldsymbol{b}^{\mathrm{e,trial}}_{n+1}$, which is given by

$$\boldsymbol{b}^{\mathrm{e,trial}}_{n+1} = \boldsymbol{F}_{n+1}\boldsymbol{G}^{\mathrm{p,trial}}_{n+1}\boldsymbol{F}^{\mathrm{t}}_{n+1}\,, \tag{4.26}$$

and noting that the material time derivative of the trial value of the plastic tensor $\boldsymbol{G}^{\mathrm{p,trial}}_{n+1}$ vanishes due to (3.13) and (4.25). Next we need to relate the left Cauchy-Green elastic tensor $\boldsymbol{b}^{\mathrm{e}}_{n+1}$ to its trial value $\boldsymbol{b}^{\mathrm{e,trial}}_{n+1}$ and the consistency parameter γ_{n+1}. Equation (4.24) is satisfied if

the corrected left Cauchy-Green elastic tensor $\boldsymbol{b}^{\mathrm{e}}$ at a time $t \in (t_n, t_{n+1}]$ relates to its trial value by

$$\boldsymbol{b}^{\mathrm{e}} = \exp\left(-2\gamma_{n+1}\,(t-t_n)\,\frac{\operatorname{dev}\boldsymbol{\tau}_{n+1}}{\|\operatorname{dev}\boldsymbol{\tau}_{n+1}\|}\right)\boldsymbol{b}^{\mathrm{e,trial}}\,, \tag{4.27}$$

where exp is the tensor exponential. Then, the use of $\boldsymbol{G}^{\mathrm{p}} = \boldsymbol{F}^{-1}\boldsymbol{b}^{\mathrm{e}}\boldsymbol{F}^{-\mathrm{t}}$ gives

$$\dot{\boldsymbol{G}}^{\mathrm{p}} = \boldsymbol{F}^{-1}\left(-2\gamma_{n+1}\frac{\operatorname{dev}\boldsymbol{\tau}_{n+1}}{\|\operatorname{dev}\boldsymbol{\tau}_{n+1}\|}\right)\exp\left(-2\gamma_{n+1}\,(t-t_n)\,\frac{\operatorname{dev}\boldsymbol{\tau}_{n+1}}{\|\operatorname{dev}\boldsymbol{\tau}_{n+1}\|}\right)\boldsymbol{F}\boldsymbol{G}^{\mathrm{p,trial}}\,, \tag{4.28}$$

so that, using also (4.26),

$$\mathscr{L}_v\boldsymbol{b}^{\mathrm{e}}_{n+1} \coloneqq \boldsymbol{F}\dot{\boldsymbol{G}}^{\mathrm{p}}\boldsymbol{F}^{\mathrm{t}} = -2\gamma_{n+1}\frac{\operatorname{dev}\boldsymbol{\tau}_{n+1}}{\|\operatorname{dev}\boldsymbol{\tau}_{n+1}\|}\,\boldsymbol{b}^{\mathrm{e}}\,. \tag{4.29}$$

Trial elastic deformation tensor. Let $\boldsymbol{X}$ be the position in the reference configuration at time step $n+1$ of a material point $\boldsymbol{X}_0 = \boldsymbol{\Upsilon}^{-1}_{0,n+1}\Big|_{\boldsymbol{X}}$. The trial elastic left Cauchy-Green deformation $\boldsymbol{b}^{\mathrm{e,trial}}_{n+1}\Big|_{\boldsymbol{X}}$ is obtained by assuming that the plastic right Cauchy-Green deformation corresponding to the material point $\boldsymbol{X}_0$ remains unchanged from the previous time step:

$$\boldsymbol{G}^{\mathrm{p(trial)}}_{0,n}\Big|_{\boldsymbol{X}_0} = \boldsymbol{G}^{\mathrm{p}}_{0,n}\Big|_{\boldsymbol{X}_0}\,. \tag{4.30}$$

In general, this is different from the plastic deformation at the previous time step at the same position in the reference configuration $\boldsymbol{G}^{\mathrm{p}}_n|_{\boldsymbol{X}}$, because the latter corresponds to a possibly different material point $\boldsymbol{X}'_0 = \boldsymbol{\Upsilon}^{-1}_{0,n}\Big|_{\boldsymbol{X}}$. To write (4.30) in terms of position in the reference configuration, we use the operator $\mathcal{M}^{t_{n+1}}_{t_n}$ (see (2.13) to keep the material point fixed:

$$\boldsymbol{G}^{\mathrm{p,trial}}_{n+1}\Big|_{\boldsymbol{X}} = \mathcal{M}^{t_{n+1}}_{t_n}\left\{\boldsymbol{G}^{\mathrm{p}}\right\}\Big|_{\boldsymbol{X}}\,. \tag{4.31}$$

Equation (3.15) then gives

$$\boldsymbol{b}^{\mathrm{e,trial}}_{n+1} = \boldsymbol{F}_{c_{(n+1)}}\boldsymbol{F}_{\mathrm{r}_{(n+1)}}\left(\mathcal{M}^{t_{n+1}}_{t_n}\left\{\boldsymbol{G}^{\mathrm{p}}\right\}\right)\boldsymbol{F}^{\mathrm{t}}_{\mathrm{r}_{(n+1)}}\boldsymbol{F}^{\mathrm{t}}_{c_{(n+1)}}\,. \tag{4.32}$$

The reference motion gradient $\boldsymbol{F}_{\mathrm{r}}$ in (4.32) requires keeping track of the material configuration as presented in [3]. There, besides the motion $\boldsymbol{\varphi}$, the material configuration is tracked as an additional variable $\boldsymbol{X}_0 = \boldsymbol{\Upsilon}^{-1}_0(\boldsymbol{X})$, which gives the reference motion gradient as $\boldsymbol{F}_{\mathrm{r}} = \left(\operatorname{Grad}\boldsymbol{\Upsilon}^{-1}_0\right)^{-1}$. This is achieved by discretization of both the motion as well as the material configuration as node variables on a mesh of the reference configuration. Following this approach, however, would limit the total reference motion possible, because large reference motion deformations may cause

excessive distortion between the material and reference configurations, causing the mesh of the material configuration to become degenerate.

To avoid this limitation on the reference motion, we seek a representation of $\boldsymbol{b}^{\mathrm{e,trial}}_{n+1}$ where motion of the reference configuration enters only in terms of the reference velocity $\boldsymbol{V}$, such that the total reference motion $\boldsymbol{\Upsilon}_0$ and the reference motion gradient $\boldsymbol{F}_{\mathrm{r}}$ are not needed.

The definition (3.14) of $\boldsymbol{B}^e$ and equation (4.31) give

$$\mathcal{M}^{t_{n+1}}_{t_n}\left\{\boldsymbol{G}^p\right\} = \left(\mathcal{M}^{t_{n+1}}_{t_n}\left\{\boldsymbol{F}^{-1}_{\mathrm{r}}\right\}\right)\left(\mathcal{M}^{t_{n+1}}_{t_n}\left\{\boldsymbol{B}^e\right\}\right)\left(\mathcal{M}^{t_{n+1}}_{t_n}\left\{\boldsymbol{F}^{-1}_{\mathrm{r}}\right\}\right)^{\mathrm{t}}. \tag{4.33}$$

This then leads to the relation

$$\begin{aligned}\mathcal{M}^{t_{n+1}}_{t_n}\left\{\boldsymbol{F}^{-1}_{\mathrm{r}}\right\} &= \left(\mathrm{Grad}_0\, \mathcal{M}^{t_{n+1}}_{t_n}\left\{\boldsymbol{X}\right\}\right)^{-1} \\ &= \boldsymbol{F}^{-1}_{\mathrm{r}}\left(\mathrm{Grad}\, \mathcal{M}^{t_{n+1}}_{t_n}\left\{\boldsymbol{X}\right\}\right)^{-1},\end{aligned} \tag{4.34}$$

so that equation (4.33) becomes

$$\mathcal{M}^{t_{n+1}}_{t_n}\left\{\boldsymbol{G}^p\right\} = \boldsymbol{F}^{-1}_{\mathrm{r}}\left(\mathrm{Grad}\, \mathcal{M}^{t_{n+1}}_{t_n}\left\{\boldsymbol{X}\right\}\right)^{-1}\left(\mathcal{M}^{t_{n+1}}_{t_n}\left\{\boldsymbol{B}^e\right\}\right)\left(\mathrm{Grad}\, \mathcal{M}^{t_{n+1}}_{t_n}\left\{\boldsymbol{X}\right\}\right)^{-\mathrm{t}}\boldsymbol{F}^{-\mathrm{t}}_{\mathrm{r}}. \tag{4.35}$$

Substitution into (4.32) then gives

$$\boldsymbol{b}^{\mathrm{e,trial}}_{n+1} = \boldsymbol{F}_{c_{(n+1)}}\boldsymbol{B}^{\mathrm{e,trial}}_{n+1}\boldsymbol{F}^{\mathrm{t}}_{c_{(n+1)}}, \tag{4.36}$$

where

$$\boldsymbol{B}^{\mathrm{e,trial}}_{n+1} = \left(\mathrm{Grad}\, \mathcal{M}^{t_{n+1}}_{t_n}\left\{\boldsymbol{X}\right\}\right)^{-1}\left(\mathcal{M}^{t_{n+1}}_{t_n}\left\{\boldsymbol{B}^e\right\}\right)\left(\mathrm{Grad}\, \mathcal{M}^{t_{n+1}}_{t_n}\left\{\boldsymbol{X}\right\}\right)^{-\mathrm{t}}. \tag{4.37}$$

With equation (2.16) this becomes

$$\boldsymbol{B}^{\mathrm{e,trial}}_{n+1} = \left(\mathrm{Grad}\, \hat{\boldsymbol{X}}_{n+1}\right)^{-1}\left(\boldsymbol{B}^e_n|_{\hat{\boldsymbol{X}}_{n+1}}\right)\left(\mathrm{Grad}\, \hat{\boldsymbol{X}}_{n+1}\right)^{-\mathrm{t}}, \tag{4.38}$$

$$\hat{\boldsymbol{X}}_{n+1} \coloneqq \mathcal{M}^{t_{n+1}}_{t_n}\left\{\boldsymbol{X}\right\} = \boldsymbol{X} - \int_{t_n}^{t_{n+1}} \mathcal{M}^{t_{n+1}}_{\tau}\left\{\boldsymbol{V}\right\}\, \mathrm{d}\tau\,. \tag{4.39}$$

4.3 Semi-discrete problem

The generalized-α method [7] is used to approximate Problem 4.1 as follows:

Problem 4.2. *For each time step t_{n+1}, given the deformation $\boldsymbol{\varphi}_n$, the reference velocity $\boldsymbol{V}_n$, and the temperature θ_n from the previous time step t_n, find the deformation $\boldsymbol{\varphi}_{n+1}$, the reference velocity $\boldsymbol{V}_{n+1}$, and the temperature θ_{n+1}, in functional spaces defined on $\Omega^{\mathcal{B}}$, $\mathcal{B} \in \{\mathrm{con}, \mathrm{tar}\}$, such that for all admissible test functions $\delta\boldsymbol{u}$ defined on $\Omega^{\mathcal{B}}$,*

$$\begin{aligned}\int_{\Omega^{\mathcal{B}}} \nabla\delta\boldsymbol{u} \colon \boldsymbol{\tau}_{n_\mathrm{f}} \,\mathrm{d}\Omega + G_{inertial} - \int_{\Omega^{\mathcal{B}}} \delta\boldsymbol{u} \cdot \boldsymbol{f}_{b n_\mathrm{f}} \,\mathrm{d}\Omega \\ - \int_{\Gamma^{\mathcal{B}}_{N_\mu}} \delta\boldsymbol{u} \cdot \boldsymbol{f}_{s,n_\mathrm{f}} \, J_\Gamma \,\mathrm{d}\Gamma - \int_{\Gamma^{\mathrm{con}}_{\mathrm{c}}} s^{\mathcal{B}} \delta\boldsymbol{u} \cdot \boldsymbol{f}_{\mathrm{c}n_\mathrm{f})} \, J_\Gamma \,\mathrm{d}\Gamma = 0\,, \end{aligned} \tag{4.40}$$

where $n_\mathrm{f} = n+1-\alpha_\mathrm{f}, n_\mathrm{m} = n+1-\alpha_\mathrm{m}$, the inertial term $G_{inertial} = \int_{\Omega^{\mathcal{B}}} \delta\boldsymbol{u} \cdot \rho_\mathrm{m} \boldsymbol{a}_{n_\mathrm{m}} \,\mathrm{d}\Omega$ is given from (4.7) by

$$\begin{aligned} G_{inertial} = &\int_{\Omega^{\mathcal{B}}} \delta\boldsymbol{u} \cdot \rho_\mathrm{m} \left\{ \left(\frac{\partial^2 \boldsymbol{\varphi}}{\partial t^2} \right)_{n_\mathrm{m}} + \left[\boldsymbol{F}_\mathrm{c} \left(\frac{\partial \boldsymbol{V}}{\partial t} \right) \right]_{n_\mathrm{m}} \right\} \mathrm{d}\Omega \\ &+ 2 \int_{\Omega^{\mathcal{B}}} \delta\boldsymbol{u} \cdot \rho_\mathrm{m} \left[\left(\frac{\partial \boldsymbol{F}_\mathrm{c}}{\partial t} \right) \boldsymbol{V} \right]_{n_\mathrm{f}} \mathrm{d}\Omega - \int_{\Omega^{\mathcal{B}}} \delta\boldsymbol{u} \cdot \left[\mathrm{Div}(\rho_\mathrm{m} \boldsymbol{V}) \boldsymbol{F}_\mathrm{c} \boldsymbol{V} \right]_{n_\mathrm{f}} \mathrm{d}\Omega \\ &- \int_{\Omega^{\mathcal{B}}} \left[(\mathrm{Grad}\ \delta\boldsymbol{u})\, \boldsymbol{V}_{n_\mathrm{f}} \right] \cdot \rho_\mathrm{m} \left(\boldsymbol{F}_\mathrm{c} \boldsymbol{V} \right)_{n_\mathrm{f}} \mathrm{d}\Omega + \int_{\Gamma^{\mathcal{B}}} \delta\boldsymbol{u} \cdot \left[\rho_\mathrm{m} \left(\boldsymbol{F}_\mathrm{c} \boldsymbol{V} \right) (\boldsymbol{V} \cdot \boldsymbol{N}) \right]_{n_\mathrm{f}} \mathrm{d}\Gamma\,, \end{aligned} \tag{4.41}$$

and such that for all admissible test functions $\delta\vartheta$ defined on $\Omega^{\mathcal{B}}$,

$$\begin{aligned}\int_{\Omega^{\mathcal{B}}} \nabla\delta\vartheta \cdot \boldsymbol{q}_{n+1} \,\mathrm{d}\Omega - \int_{\Omega^{\mathcal{B}}} \delta\vartheta \left[\mathcal{R}_{b(n+1)} + \mathcal{D}_{\mathrm{mech}(n+1)} - \mathcal{H}_{n+1} \right] \mathrm{d}\Omega \\ + \int_{\Omega^{\mathcal{B}}} \delta\vartheta \; c\dot{\theta}_{n+1} \,\mathrm{d}\Omega - \int_{\Gamma^{\mathcal{B}}_{N_\theta}} \delta\vartheta \; \mathcal{R}_{s(n+1)} \; \frac{J_\Gamma}{J} \,\mathrm{d}\Gamma \\ - \int_{\Gamma^{\mathrm{con}}_{\mathrm{c}}} \delta\vartheta \; \left(\mathcal{D}_{fric(n+1)} + s^{\mathcal{B}} q_{hc(n+1)} \right) \; \frac{J_\Gamma}{J} \,\mathrm{d}\Gamma = 0\,. \end{aligned} \tag{4.42}$$

4.4 Mechanical-thermal operator splitting

Following [29], an operator splitting approach is used to approximate the coupled thermomechanical Problem 4.2. At each time step, three smaller problems are solved. The first problem, a mechanical one, is solved for a motion field $\boldsymbol{\varphi}^{(\mathrm{pre})}_{n+1}$ and a reference velocity field $\boldsymbol{V}^{(\mathrm{pre})}_{n+1}$ with the temperature field kept fixed at θ_n. The middle problem is solved for the updated thermal field θ_{n+1} with the deformation and reference velocity fixed, respectively, as $\boldsymbol{\varphi}^{(\mathrm{pre})}_{n+1}$ and $\boldsymbol{V}^{(\mathrm{pre})}_{n+1}$. The time step is then completed by solving the third problem for the updated motion $\boldsymbol{\varphi}_{n+1}$ and reference velocity $\boldsymbol{V}_{n+1}$ with the thermal field fixed as θ_{n+1}.

The first and third problems are as follows.

Problem 4.3. *For each time step $n+1$, given the deformation $\boldsymbol{\varphi}_n$, the reference velocity $\boldsymbol{V}_n$, and the temperature θ_n from the previous time step t_n, assuming the updated temperature remains unchanged (at θ_n in the first mechanical sub-step, and at θ_{n+1} after the thermal sub-step is solved), find the deformation $\boldsymbol{\varphi}_{n+1}^{(\mathrm{pre})}$ and the reference velocity $\boldsymbol{V}_{n+1}^{(\mathrm{pre})}$ such that, for all admissible test functions $\delta\boldsymbol{u}$ defined on $\Omega^{\mathcal{B}}$, $\mathcal{B} \in \{\mathrm{con}, \mathrm{tar}\}$,*

$$\int_{\Omega^{\mathcal{B}}} \nabla\delta\boldsymbol{u} \colon \boldsymbol{\tau}_{n_{\mathrm{f}}} \,\mathrm{d}\Omega + G_{inertial} - \int_{\Omega^{\mathcal{B}}} \delta\boldsymbol{u} \cdot \boldsymbol{f}_{b,n_{\mathrm{f}}} \,\mathrm{d}\Omega \\ - \int_{\Gamma^{\mathcal{B}}_{N_\mu}} \delta\boldsymbol{u} \cdot \boldsymbol{f}_{s,n_{\mathrm{f}}} \, J_\Gamma \mathrm{d}\Gamma - \int_{\Gamma^{\mathrm{con}}_{\mathrm{c}}} s^{\mathcal{B}} \delta\boldsymbol{u} \cdot \boldsymbol{f}_{\mathrm{c},n_{\mathrm{f}}} \, J_\Gamma \mathrm{d}\Gamma = 0 \,, \tag{4.43}$$

where the inertial term $G_{inertial}$ is given y (4.41).

The second problem is as follows.

Problem 4.4. *For each time step t_{n+1}, given the deformation $\boldsymbol{\varphi}_n$, the reference velocity $\boldsymbol{V}_n$, and the temperature θ_n from the previous time step t_n, and given an updated deformation $\boldsymbol{\varphi}_{n+1}^{(\mathrm{pre})}$ and reference velocity $\boldsymbol{V}_{n+1}^{(\mathrm{pre})}$, find the temperature θ_{n+1} such that, for all admissible test functions $\delta\vartheta$ defined on $\Omega^{\mathcal{B}}$, $\mathcal{B} \in \{\mathrm{con}, \mathrm{tar}\}$,*

$$\int_{\Omega^{\mathcal{B}}} \nabla\delta\vartheta \cdot \boldsymbol{q}_{n+1} \,\mathrm{d}\Omega - \int_{\Omega^{\mathcal{B}}} \delta\vartheta \left[\mathcal{R}_{b_{(n+1)}} + \mathcal{D}_{\mathrm{mech}_{(n+1)}} - \mathcal{H}_{n+1}\right] \mathrm{d}\Omega \\ + \int_{\Omega^{\mathcal{B}}} \delta\vartheta \; c\dot{\theta}_{n+1} \,\mathrm{d}\Omega - \int_{\Gamma^{\mathcal{B}}_{N_\theta}} \delta\vartheta \; \mathcal{R}_{s_{(n+1)}} \; \frac{J_\Gamma}{J} \,\mathrm{d}\Gamma - \int_{\Gamma^{\mathrm{con}}_{\mathrm{c}}} \delta\vartheta \; \left(\mathcal{D}_{fric(n+1)} + s^{\mathcal{B}} q_{hc_{(n+1)}}\right) \; \frac{J_\Gamma}{J} \,\mathrm{d}\Gamma = 0 \,. \tag{4.44}$$

4.5 Regularization and Augmented-Lagrangian iteration

The term in (4.43) involving contact traction must satisfy the complementarity conditions (3.43) and (3.3). An augmented Lagrangian approach is adopted, as described in [28], and which involves iteratively updating an approximate value of the contact force.

The contact force $\boldsymbol{f}_{\mathrm{c}}$ is given by its normal and tangential components, f_N and $\boldsymbol{f}_T$; that is,

$$\boldsymbol{f}_{\mathrm{c}_{(n+1)}} = -f_{N_{(n+1)}} \boldsymbol{n} + \boldsymbol{f}_{T_{(n+1)}} \,, \quad f_{N_{(n+1)}} = -\boldsymbol{f}_{\mathrm{c}_{(n+1)}} \cdot \boldsymbol{n} \,, \quad \boldsymbol{f}_{T_{(n+1)}} = (\boldsymbol{1} - \boldsymbol{n} \otimes \boldsymbol{n}) \boldsymbol{f}_{\mathrm{c}_{(n+1)}} \,. \tag{4.45}$$

At each augmented Lagrangian iteration $l+1$, the updated normal contact force is given by

$$f_{N_{(n+1)}}^{(l+1)} = \begin{cases} f_{N_{(n+1)}}^{(l)} + \epsilon_N g & \text{if } g > 0\,, \\ f_{N_{(n+1)}}^{(l)} & \text{otherwise}\,. \end{cases} \tag{4.46}$$

The updated tangential contact force is computed by first assuming that contact satisfies the slip condition, and computing a trial value:

$$\boldsymbol{f}_{T_{(n+1)}}^{(l+1)(\text{trial})} = \boldsymbol{f}_{T_{(n+1)}}^{(l)} + \epsilon_T \boldsymbol{v}_s\,. \tag{4.47}$$

The friction stick limit $\Phi\left(\boldsymbol{f}_T, f_N\right)$ is then evaluated from $(3.44)_1$, correcting the trial value if necessary:

$$\boldsymbol{f}_{T_{(n+1)}}^{(l+1)} = \begin{cases} \boldsymbol{f}_{T_{(n+1)}}^{(l+1)(\text{trial})} & \text{if } \Phi\left(\boldsymbol{f}_{T_{(n+1)}}^{(l+1)(\text{trial})}, f_{N_{(n+1)}}^{(l+1)}\right) \leq 0\,, \\ f_{\text{slip}} \boldsymbol{v}_s / \left[\|\boldsymbol{v}_s\| + \epsilon_{\text{reg}}\right] & \text{otherwise}\,. \end{cases} \tag{4.48}$$

Here f_{slip} is the stick limit, and ϵ_{reg} is a small positive regularization factor used to avoid numerical errors at small slip velocities.

The augmented Lagrangian iteration is continued until the contact constraints are met, that is, the penetration is smaller than a predefined threshold, $g \leq \varepsilon_{\text{penetration}}$, and the tangential contact constraint is satisfied in that either slip occurs and $\Phi\left(\boldsymbol{f}_{T_{(n+1)}}^{(l+1)}, f_{N_{(n+1)}}^{(l+1)}\right) = 0$; or the slip velocity is smaller than a predefined threshold: $\|\boldsymbol{v}_s\| < \varepsilon_{\text{slip}}$.

4.6 Finite element discretization

The approximate solution $\left(\boldsymbol{\varphi}^h, \boldsymbol{V}^h, \theta^h\right)$ is sought in finite dimensional subspaces of the function spaces on which the exact solution $(\boldsymbol{\varphi}, \boldsymbol{V}, \theta)$ is defined. These finite dimensional subspaces have bases $\left\{\boldsymbol{\phi}_i^{\boldsymbol{\varphi}}\right\}_{i=1}^{N_\varphi}$, $\left\{\boldsymbol{\phi}_i^{\boldsymbol{V}}\right\}_{i=1}^{N_V}$, and $\left\{\phi_i^\theta\right\}_{i=1}^{N_\theta}$, where $\boldsymbol{\phi}_i^{\boldsymbol{\varphi}}$ and $\boldsymbol{\phi}_i^{\boldsymbol{V}}$ are vector-valued while ϕ_i^θ are scalar-valued, and where N_φ, N_V and N_θ are the dimensions of the respective function subspaces. A mixed finite element approach is used to include the Jacobian and pressure as additional unknown variables to avoid volumetric locking. The scalar shape functions are chosen to be discontinuous across element boundaries and to have lower polynomial order than the motion

basis functions $\boldsymbol{\phi}_i^{\boldsymbol{\varphi}}$. The lower order discretised deformation Jacobian $\bar{J}^h$ is obtained by least-squares projection of the discretised deformation Jacobian $J^h = \det\left(\mathrm{Grad}\,\boldsymbol{\varphi}^h\right)$ onto the discrete subspace; that is,

$$\bar{J}^h|_{\Omega_e} = \phi_i^{\mathrm{p}} \left(\int_{\Omega_e} \phi_i^{\mathrm{p}}\, \phi_j^{\mathrm{p}}\, \mathrm{d}\Omega \right)^{-1} \int_{\Omega_e} \phi_j^{\mathrm{p}}\, J^h\, \mathrm{d}\Omega\,. \tag{4.49}$$

Furthermore, the mixed basis functions ϕ_i^{p} are chosen such that the support of each is completely contained in one cell, such that (4.49) can be solved in each cell independently of the rest of the mesh. The pressure is then given, using (3.32b), by

$$\bar{p}^h|_{\Omega_e} = \phi_i^{\mathrm{p}} \left(\int_{\Omega_e} \phi_i^{\mathrm{p}}\, \phi_j^{\mathrm{p}}\, \mathrm{d}\Omega \right)^{-1} \int_{\Omega_e} \phi_j^{\mathrm{p}}\, \kappa \left((\bar{J}^h)^2 - 1 \right) \mathrm{d}\Omega\,. \tag{4.50}$$

The finite element mechanical and thermal problems are as follows.

Problem 4.5. *For each time step t_{n+1}, given the deformation $\boldsymbol{\varphi}_n^h$, the reference velocity $\boldsymbol{V}_n^h$, and the temperature θ_n^h from the previous time step t_n, and given an updated temperature θ_{n+1}^h, find the deformation $\boldsymbol{\varphi}_{n+1}^h$ and the reference velocity $\boldsymbol{V}_{n+1}^h$ such that, for any test function $\delta\boldsymbol{u}^h$,*

$$\begin{aligned} &\int_{\Omega_h^{\mathcal{B}}} \nabla\delta\boldsymbol{u}^h \colon (\mathrm{dev}\,\boldsymbol{\tau}_{n_{\mathrm{f}}}^h + \bar{p}_{n_{\mathrm{f}}}^h\,\mathbf{1})\,\mathrm{d}\Omega + G_{inertial}^h - \int_{\Omega_h^{\mathcal{B}}} \delta\boldsymbol{u}^h \cdot \boldsymbol{f}_{\mathrm{b},n_{\mathrm{f}}}\,\mathrm{d}\Omega \\ &\qquad - \int_{\Gamma_{hN_\mu}^{\mathcal{B}}} \delta\boldsymbol{u}^h \cdot \boldsymbol{f}_{\mathrm{s},n_{\mathrm{f}}}\, J_\Gamma^h\,\mathrm{d}\Gamma - \int_{\Gamma_{hc}^{\mathrm{con}}} s^{\mathcal{B}}\delta\boldsymbol{u}^h \cdot \boldsymbol{f}_{\mathrm{c},n_{\mathrm{f}}}^h\, J_\Gamma^h\,\mathrm{d}\Gamma = 0\,, \end{aligned} \tag{4.51}$$

where $\boldsymbol{\tau}_{n_{\mathrm{f}}}$ is the stress computed from the discretised mechanical and thermal fields, and

$$\begin{aligned} G_{inertial}^h = &\int_{\Omega_h^{\mathcal{B}}} \delta\boldsymbol{u}^h \cdot \rho_{\mathrm{m}} \left\{ \left(\frac{\partial^2\boldsymbol{\varphi}^h}{\partial t^2} \right)_{n_{\mathrm{m}}} + \left[\boldsymbol{F}_{\mathrm{c}} \left(\frac{\partial \boldsymbol{V}^h}{\partial t} \right) \right]_{n_{\mathrm{m}}} \right\} \mathrm{d}\Omega \\ &+ 2\int_{\Omega_h^{\mathcal{B}}} \delta\boldsymbol{u}^h \cdot \rho_{\mathrm{m}} \left[\left(\frac{\partial \boldsymbol{F}_{\mathrm{c}}^h}{\partial t} \right) \boldsymbol{V}^h \right]_{n_{\mathrm{f}}} \mathrm{d}\Omega - \int_{\Omega_h^{\mathcal{B}}} \delta\boldsymbol{u}^h \cdot \left[\mathrm{Div}(\rho_{\mathrm{m}}\boldsymbol{V}^h)\boldsymbol{F}_{\mathrm{c}}^h\boldsymbol{V}^h \right]_{n_{\mathrm{f}}} \mathrm{d}\Omega \\ &- \int_{\Omega_h^{\mathcal{B}}} \left(\left(\mathrm{Grad}\;\delta\boldsymbol{u}^h \right) \boldsymbol{V}_{n_{\mathrm{f}}}^h \right) \cdot \rho_{\mathrm{m}} \left(\boldsymbol{F}_{\mathrm{c}}^h \boldsymbol{V}^h \right)_{n_{\mathrm{f}}} \mathrm{d}\Omega + \int_{\Gamma_h^{\mathcal{B}}} \delta\boldsymbol{u}^h \cdot \left[\rho_{\mathrm{m}} \left(\boldsymbol{F}_{\mathrm{c}}^h \boldsymbol{V}^h \right) \left(\boldsymbol{V}^h \cdot \boldsymbol{N}^h \right) \right]_{n_{\mathrm{f}}} \mathrm{d}\Gamma\,. \end{aligned} \tag{4.52}$$

Problem 4.6. *For each time step t_{n+1}, given the deformation $\boldsymbol{\varphi}_n^h$, the reference velocity $\boldsymbol{V}_n^h$, and the temperature $\theta_n^h = \sum_{i=1}^{N_\theta} \phi_i^\theta\,(\Theta_i)_n$ from the previous time step t_n, and given an updated deformation $\boldsymbol{\varphi}_{n+1}^h$ and reference velocity $\boldsymbol{V}_{n+1}^h$, find the temperature $\theta_{n+1}^h = \sum_{i=1}^{N_\theta} \phi_i^\theta\,(\Theta_i)_{n+1}$ such that, for any test function $\delta\vartheta^h$,*

$$\begin{aligned} &\int_{\Omega_h^{\mathcal{B}}} \nabla\delta\vartheta^h \cdot \boldsymbol{q}_{n+1}^h\,\mathrm{d}\Omega - \int_{\Omega_h^{\mathcal{B}}} \delta\vartheta^h \left[\mathcal{R}_{b_{(n+1)}}^h + \mathcal{D}_{\mathrm{mech}_{(n+1)}}^h - \mathcal{H}_{n+1}^h \right] \mathrm{d}\Omega + \int_{\Omega_h^{\mathcal{B}}} \delta\vartheta^h\, c\dot{\theta}_{n+1}^h\,\mathrm{d}\Omega \\ &- \int_{\Gamma_{hN_\theta}^{\mathcal{B}}} \delta\vartheta^h\, \mathcal{R}_{s_{(n+1)}}^h\, \frac{J_\Gamma^h}{J^h}\,\mathrm{d}\Gamma - \int_{\Gamma_{hc}^{\mathrm{con}}} \delta\vartheta^h \left(\mathcal{D}_{fric_{(n+1)}}^h + s^{\mathcal{B}} q_{hc_{(n+1)}}^h \right) \frac{J_\Gamma^h}{J^h}\,\mathrm{d}\Gamma = 0\,, \end{aligned} \tag{4.53}$$

where the thermal flux $\boldsymbol{q}^h_{n+1}$ *is computed in terms of the discrete thermal field* θ^h_{n+1}.

5 Benchmark problems and application to friction welding

The various features of the plasticity solver are now validated using a series of benchmark problems and then applied to the problem of friction welding to elucidate important features relevant to thermomechanical problems undergoing large deformations and subject to contact constraints.

5.1 Thermally-triggered necking of a circular bar

The problem of the necking of a circular bar has been used to validate both finite strain elasto-plasticity [2] and thermoplasticity solvers [23, 36, 29, 17]. The thermomechanical problem involves a tensile test of a circular bar with an initial radius of 6.4 mm and a height of 106.7 mm elongated by 16 mm, as shown in Figure 4(a). A thermal convection boundary condition is applied to the mechanically unconstrained boundaries where the ambient temperature is 293 K and the convection coefficient is given as $17.5 \times 10^{-6}\,\mathrm{J\,mm^{-2}\,s^{-1}\,K^{-1}}$. The thermal initial condition is a homogeneous temperature of 293 K. The exponential hardening law is used, which is given by

$$\sigma^y = y_0 f_0(\theta) + h f_h(\theta)\alpha + y_{0,\infty} f_h(\theta)\left[1 - \exp(-\delta\alpha)\right] , \tag{5.1a}$$

$$f_0(\theta) = \left[1 - \omega_0\left(\theta - \theta_0\right)\right] , \qquad f_h(\theta) = \left[1 - \omega_h\left(\theta - \theta_0\right)\right] , \tag{5.1b}$$

and the material parameters used are specified in Table 1. The dissipation factor χ is an empirical quantity that represents mechanical dissipation as a proportion of the total plastic power [29]. Rotational symmetry is used to reduce the three-dimensional problem to an axisymmetric one. Mirror symmetry is used to further reduce the problem so that it is only necessary to simulate one quadrant of the bar.

Localised heat generation occurs at the center of the bar due to plastic dissipation. This results in a reduction in the yield strength associated with thermoplastic softening and the localisation

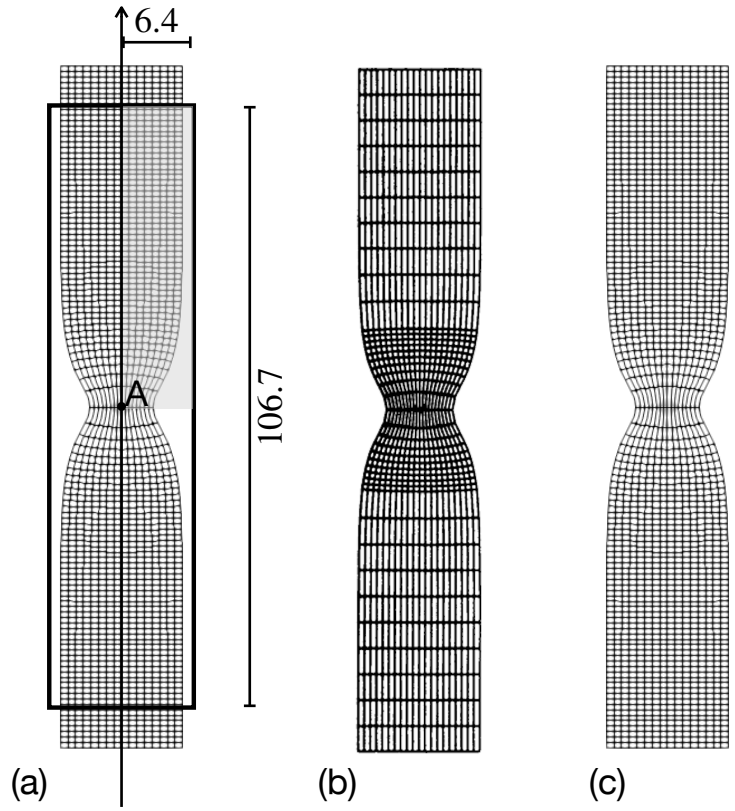

Figure 4: The problem of thermally triggered necking of a circular bar: (a) the problem setup, (b) the deformed domain after an elongation of 14.08 mm from [29], and (c) the Lagrangian formulation.

of the deformation. A comparison of the outline of the deformed body after an elongation by 14.08 mm predicted by the Lagrangian approach of [29] and the Lagrangian solver developed here are shown in Figure 4(b) and (c), respectively.

Figure 5 shows the predicted increase in surface temperature at the midpoint (point A in Figure 4), along with the results reported in [29]. The temperature distribution at different elongation values is shown in Figure 6. The deformed configuration, the temperature distributions, and the elongation at the onset of necking are all in good agreement with the benchmark results [17, 29].

The performance of the ALE formulation is now assessed. The evolution of the temperature at point A is also shown in Figure 5 together with the Lagrangian results. The results compare

Parameter	Value	Parameter	Value
Bulk modulus κ	$164\,206\,\mathrm{Nmm}^{-2}$	Density ρ	$7.8 \times 10^{-9}\,\mathrm{Nmm}^{-4}\mathrm{s}^2$
Shear modulus μ	$801\,938\,\mathrm{Nmm}^{-2}$	Thermal expansion coeff. α	$1 \times 10^{-5}\,\mathrm{K}^{-1}$
Flow stress y_0	$450\,\mathrm{Nmm}^{-2}$	Thermal conductivity k	$4.5 \times 10^{-2}\,\mathrm{Jmm}^{-1}\mathrm{s}^{-1}\mathrm{K}^{-1}$
Linear hardening h	$129.24\,\mathrm{Nmm}^{-2}$	Volumetric heat capacity c	$3.588 \times 10^{-3}\,\mathrm{Jmm}^{-3}\mathrm{K}^{-1}$
Saturation hardening $y_{0,\infty}$	$715\,\mathrm{Nmm}^{-2}$	Flow stress softening ω_0	$0.002\,\mathrm{K}^{-1}$
Hardening exponent δ	16.93	Hardening softening ω_h	$0.002\,\mathrm{K}^{-1}$
Dissipation factor χ	0.9		

Table 1: Material parameters for the thermally triggered necking benchmark

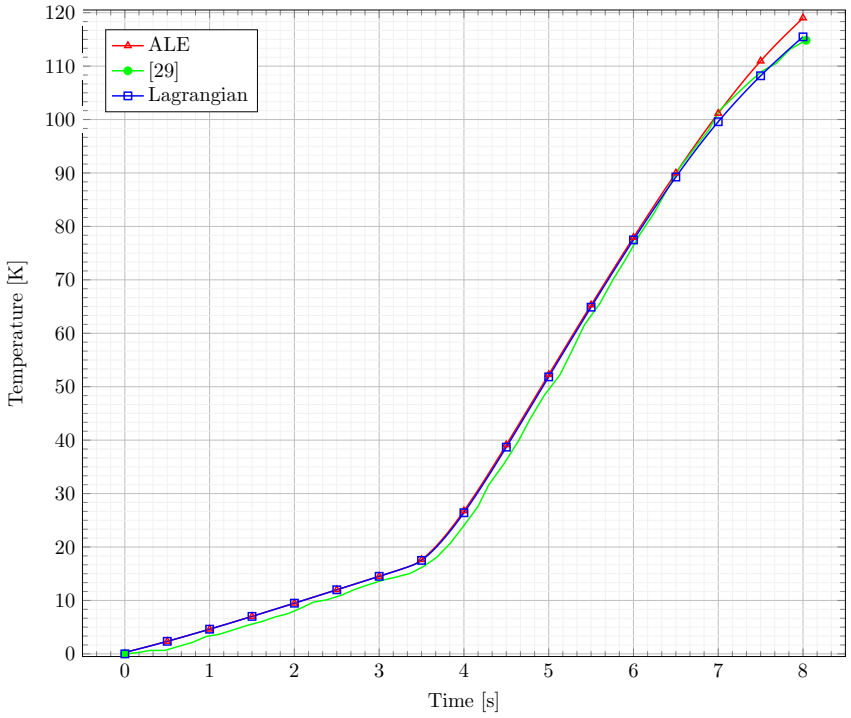

Figure 5: Comparison of the evolution of the temperature at point A for the thermally triggered necking problem using the ALE and Lagrangian approaches as well as the results from [29]

well with only a small deviation occurring after 7 s. The deformed configurations obtained using the ALE and Lagrangian formulations at an elongation of 14.08 mm are shown on either side of the symmetry axis in Figure 7. In the fully Lagrangian simulation, the elements within the necking region undergo significant elongation. In the ALE simulation, by contrast, the mesh

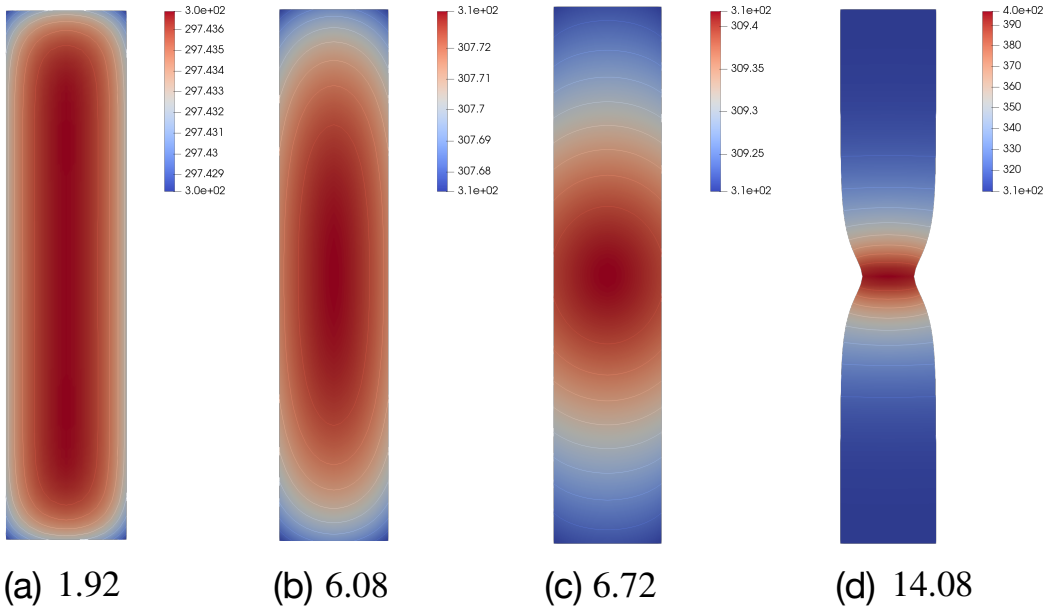

Figure 6: Thermally triggered necking of a circular bar: Temperature distribution at four elongation values.

quality within the necking region remains high throughout the weld.

Figure 8 shows the distribution of the temperature, equivalent plastic strain and the von Mises stress obtained using the ALE and Lagragian formulations and compares them to a Lagrangian solution produced with a fine mesh. For all these comparisons, the ALE simulation produces as accurate or more accurate results than the Lagrangian simulation with the same initial mesh, where accuracy is evaluated against the results of the simulation run with a fine mesh. In particular, the von Mises stress distribution obtained using the ALE formulation appears smoother and less chequered.

Of the total computation time to complete the ALE simulation, 34.2% was spent on the solution of the mesh motion problem and the remapping of the nodal and quadrature point fields, 61.6% was spent on the solution of the mechanical sub-steps, and 4.2% was spent on the thermal sub-step. The total computation time for the ALE solver was 60% longer than the Lagrangian solver, in which 93.9% of the total computation time was spent on the mechanical sub-steps and 6.1% was spent on the thermal sub-steps. There is no significant difference in the number of Newton steps required to solve the mechanical sub-steps between the different approaches.

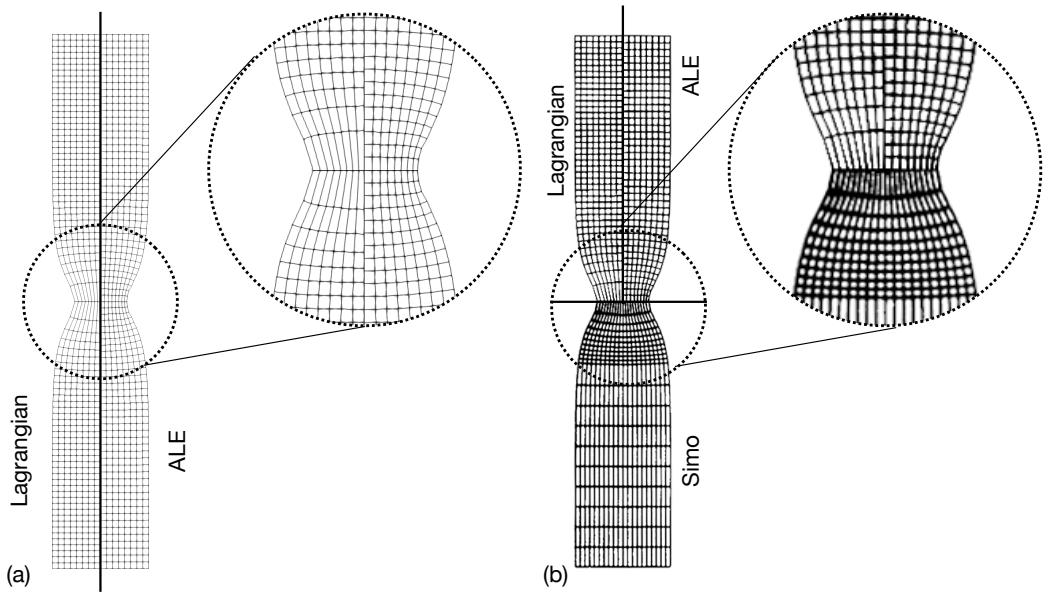

Figure 7: A comparison of the Lagrangian and ALE solutions after an elongation of 14.08 mm is shown in (a). A comparison with the results from [29] is shown in (b).

5.2 Dynamic Impact of a Circular Bar

The Taylor anvil on rod impact test [31] is commonly used to characterise the dynamic behaviour of metals at elevated temperatures and high strain rates. It is also a useful test to evaluate dynamic solvers and hydrocodes [see e.g. 14]. The problem involves a cylindrical rod with a radius of 3.81 mm and a height of 25.4 mm which is subjected to an impact load by collision with a rigid obstacle at an initial velocity of 1.9×10^5 mm/s. The convective boundary condition at the surface is omitted as the duration of the impact is so short that convection heat transfer is negligible. The Johnson-Cook model (3.37) is used to describe the rod material, with the material parameters listed in Table 2.

The deformed body at the end of the simulation using the Lagrangian approach detailed here is shown in Figure 9(a). The final deformation is nearly identical to that obtained by the hydrocode reported in [14].

In addition to the standard benchmark simulation, which considers impact with a rigid obstacle, the simulation is also performed with a deformable obstacle with the same material properties

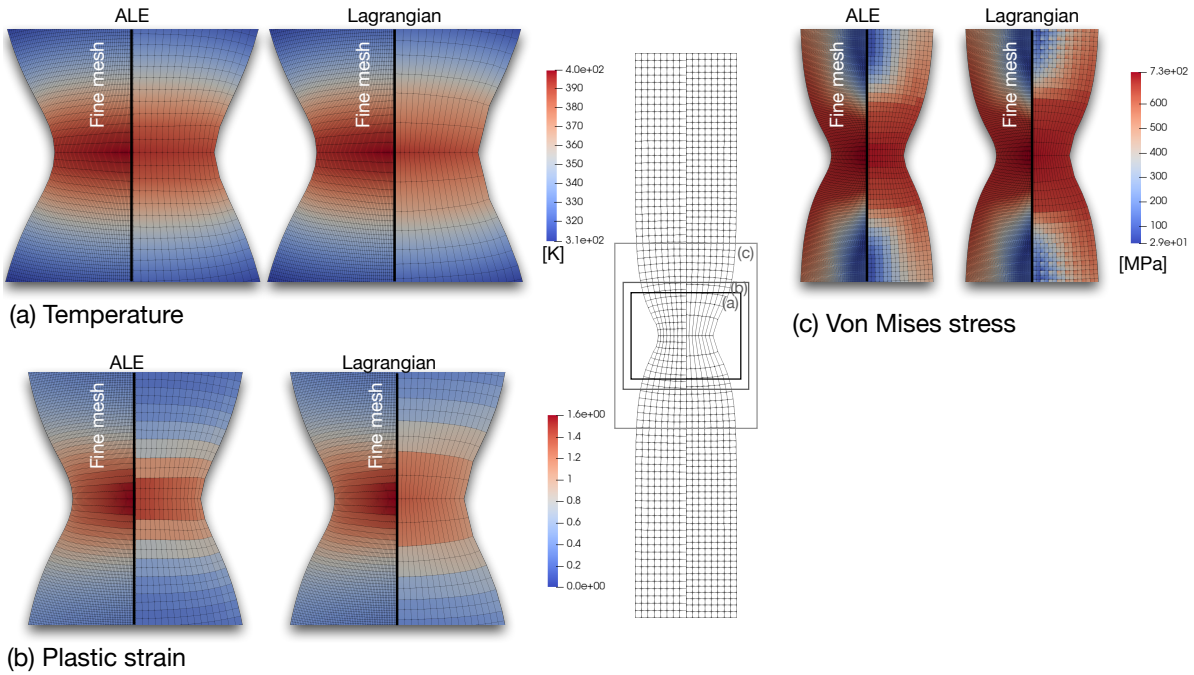

Figure 8: Comparison of (a) the temperature, (b) the equivalent plastic strain and (c) the von Mises stress distribution obtained using the ALE and Lagrangian approaches. A fine-mesh Lagrangian solution provides the reference solution.

as the rod. This additional test case assesses the various formulations abilities to resolve contact at high strain rates. The resulting deformed cylindrical rod and obstacle at the end of the simulation obtained using the Lagrangian approach are shown in Figure 9(b).

The Taylor impact benchmark is now used to test the ALE formulation. Figure 10 shows, on either side of the midline, the final deformed configuration that result when the simulation is run with or without the ALE steps, as well as the temperature, the pressure, and the von Mises stress distributions. As expected, the mesh distortion near the impact region is higher in the Lagrangian simulation than the ALE one. The results of the Lagrangian and ALE simulations of the problem are otherwise similar.

Parameter	Value	Parameter	Value
Bulk modulus κ	$103\,300\,\mathrm{N\,mm^{-2}}$	Reference temperature θ_R	$293.15\,\mathrm{K}$
Shear modulus μ	$47\,690\,\mathrm{N\,mm^{-2}}$	Melting temperature θ_M	$1356\,\mathrm{K}$
Johnson-Cook A	$89.7\,\mathrm{N\,mm^{-2}}$	Density ρ	$8.96 \times 10^{-9}\,\mathrm{N\,mm^{-4}\,s^2}$
Johnson-Cook B	$291.87\,\mathrm{N\,mm^{-2}}$	Thermal expansion coefficient α	$1 \times 10^{-5}\,\mathrm{K^{-1}}$
Johnson-Cook C	0.025	Thermal conductivity k	$4.5 \times 10^{-2}\,\mathrm{J\,mm^{-1}\,s^{-1}\,K^{-1}}$
Johnson-Cook m	1.09	Volumetric heat capacity c	$3.588 \times 10^{-3}\,\mathrm{J\,mm^{-3}\,K^{-1}}$
Johnson-Cook n	0.31	Dissipation factor χ	0.9
Reference strain rate $\dot{\varepsilon}_0$	$1\,\mathrm{s^{-1}}$		

Table 2: Material parameters for the dynamic impact of a circular bar problem

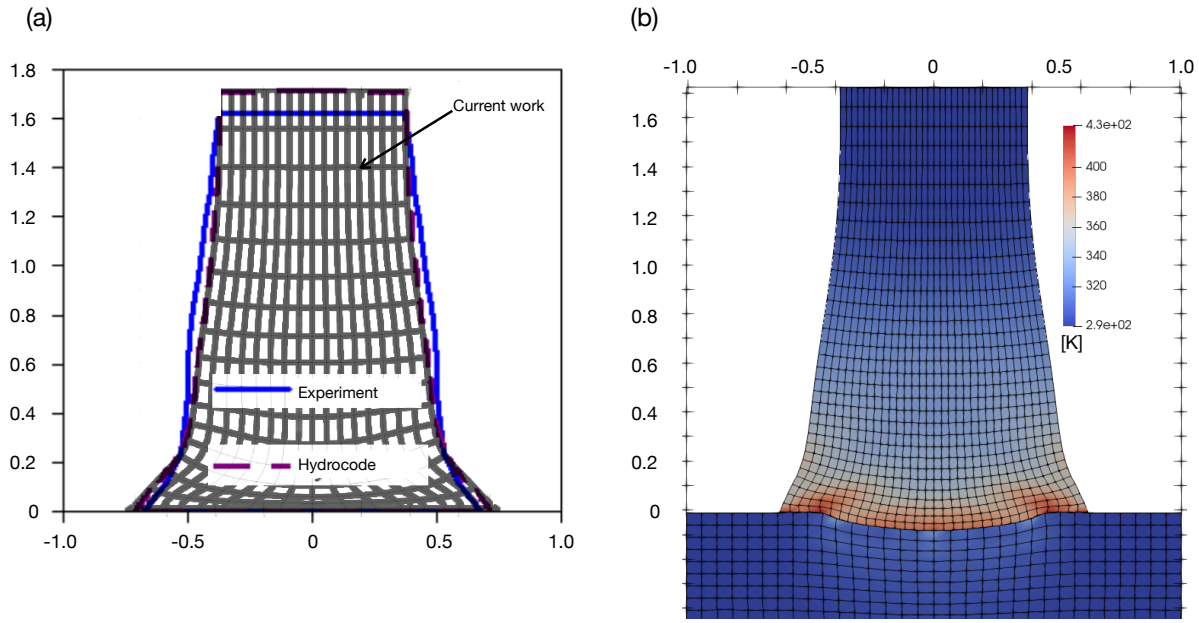

Figure 9: In (a), a comparison of the deformed domains obtained using a Lagrangian approach developed in the current work with a hydrocode and experiment [14] for a rigid obstacle. The final configuration obtained using the Lagrangian approach and a deformable body with the temperature field superimposed is shown in (b).

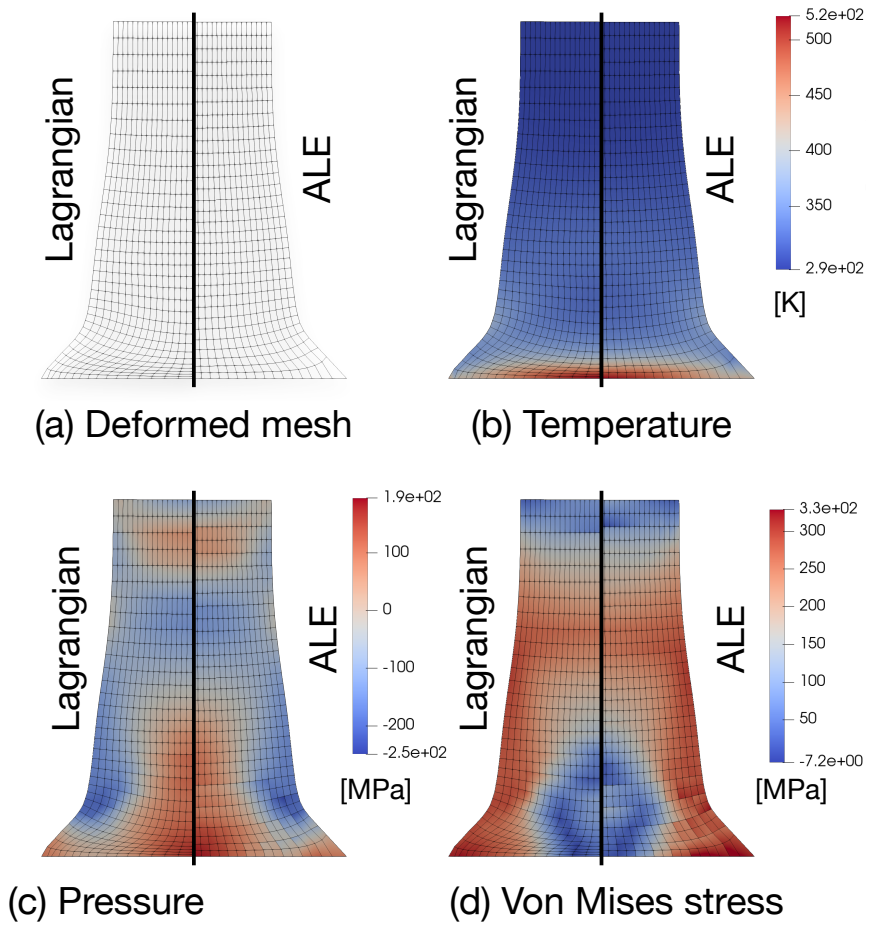

Figure 10: Comparison of the Lagrangian and ALE approaches for the problem of dynamic impact of a circular bar. The deformed mesh, the temperature, the pressure and the von Mises stress distribution are shown in (a), (b), (c) and (d), respectively.

5.3 Friction welding problem

The simulation of a direct drive friction weld between two similar hollow bars with an outer diameter of 50 mm and an inner diameter of 25 mm is now described. The workpiece geometry and weld process parameters are based on the weld presented by Schmicker et al. [26].

Based on the weld process parameters [26], the mechanical boundary conditions are a constant rotational speed of 800 rpm and a constant downward pressure of $40\,\mathrm{N/mm^2}$ throughout the weld. The friction coefficient is set to 0.3. The only thermal boundary condition imposed is a convection boundary condition with a convection coefficient of $20 \times 10^{-6}\,\mathrm{J/mm^2sK}$ on the boundaries of the two workpieces and an ambient temperature of 293 K, which is also set as the thermal initial condition.

During the weld simulation, the downward force is primarily balanced by the normal contact force. As described in Section 2.2, the normal contact force at each augmented Lagrangian step is made up of two components: the penalty component and the accumulated augmented Lagrangian component from the previous steps. The penalty component, in turn, is modified at each Newton step according to the penetration and the normal contact penalty factor. If the contact penalty factor is sufficiently large, then the magnitude of the total normal contact force may overshoot that of the applied downward force in some intermediate iterations of the Newton-Raphson loop. If the resulting incremental displacement is such that the gap between the contactor and target surfaces is positive, then the Newton-Raphson method may fail to converge, because the force balance would require, at least as an intermediate measure, the application of a tensile contact force, which would violate the normal contact constraints. To address this issue without incurring a large change in the number of augmented Lagrangian steps or the time increment, a unidirectional spring boundary condition in combination with the downward force boundary condition is applied. At each point on the upper surface of the contactor, if the displacement is in the opposite direction to the applied downward force, then a small downward force proportional to the displacement is added. If the displacement is in the same direction as the downward force, then no additional force is applied.

Following [26], the material response is approximated using the modified Johnson-Cook model (3.40-3.41. The material is assumed to be a perfectly viscoplastic solid, with the stress vanishing

as the strain rate approaches zero and the elastic behaviour of the material is approximated by using a very large viscosity value in the stress range below the yield strength. By contrast, in the return-mapping approach employed here, the material remains elastic when the stress is below the yield strength of the material. With this modification, the flow rule only applies at stresses above the yield strength. The material parameter values used are listed in Table 3.

Parameter	Value	Parameter	Value
Bulk modulus κ	$158\,700\,\mathrm{N/mm^2}$	Reference strain rate $\dot{\varepsilon}_0$	$1\,\mathrm{s^{-1}}$
Shear modulus μ	$77\,520\,\mathrm{N/mm^2}$	Density ρ	$7.87 \times 10^{-6}\,\mathrm{kg/mm^{-3}}$
A	$235\,\mathrm{N/mm}$	Thermal expansion coefficient α	$1 \times 10^{-5}\,\mathrm{K^{-1}}$
B	$0\,\mathrm{N/mm^2}$	Thermal conductivity k	$3.5 \times 10^{-2}\,\mathrm{J/mm\,s\,K}$
d	0.2	Volumetric heat capacity c	$6.445 \times 10^{-3}\,\mathrm{J/mm^3\,K}$
m	1.5	Dissipation factor χ	0.9
n	1	Upper saturation viscosity μ_0	$1 \times 10^{22}\,\mathrm{N\,s/mm^2}$
Reference temp. θ_R	$293.15\,\mathrm{K}$	Lower saturation viscosity μ_∞	$1 \times 10^{-4}\,\mathrm{N\,s/mm^2}$
Melting temp. θ_M	$1693.15\,\mathrm{K}$		

Table 3: Material parameters for the direct drive welding of a hollow bars problem

Adaptive Time Stepping. During the weld, where plastic deformation takes place at high strain rates, the time increment required to accurately resolve the material response is orders of magnitude smaller than that required during the conditioning stage, where the deformation is primarily elastic. For this reason, an adaptive time stepping procedure is implemented. In this procedure, the time increment size in increased by a small percentage each time step up to a predetermined maximum value. When a convergence failure is detected, the time increment size is halved and computation of that time step is restarted. This approach saves computational time during the early stages of the weld by using a larger time increment value, and a sufficiently small time increment value is used later in the weld when it is necessary.

Simulation Results. The deformation and temperature distributions at various stages of the weld, obtained using the ALE formulation, are shown in Figure 11. A comparison with [26] of the temperature distribution superimposed upon the deformed shape at the end of the weld is shown in Figure 12. It shows good qualitative agreement at the weld interface, with the

temperature in both simulations approaching, but not exceeding, the melting temperature of 1420 °C.

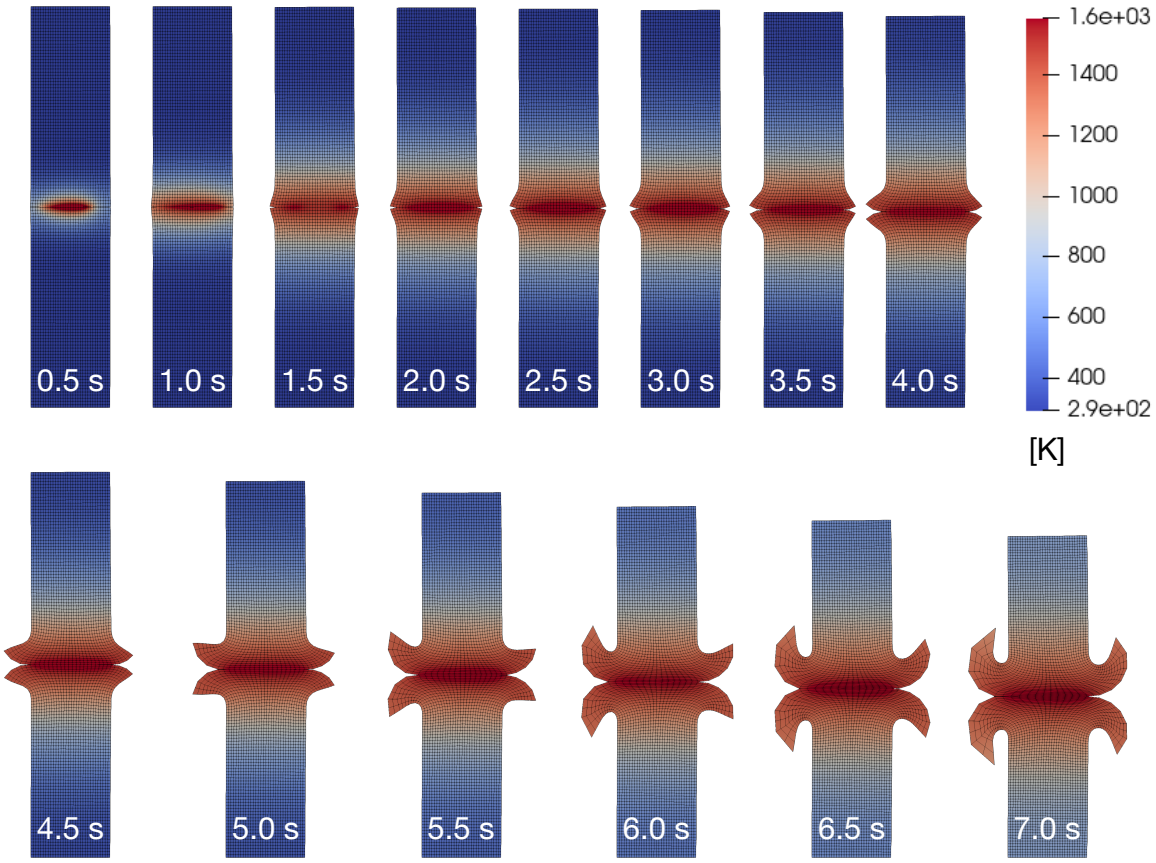

Figure 11: The evolution of the weld obtained using the ALE formulation with the temperature field superimposed.

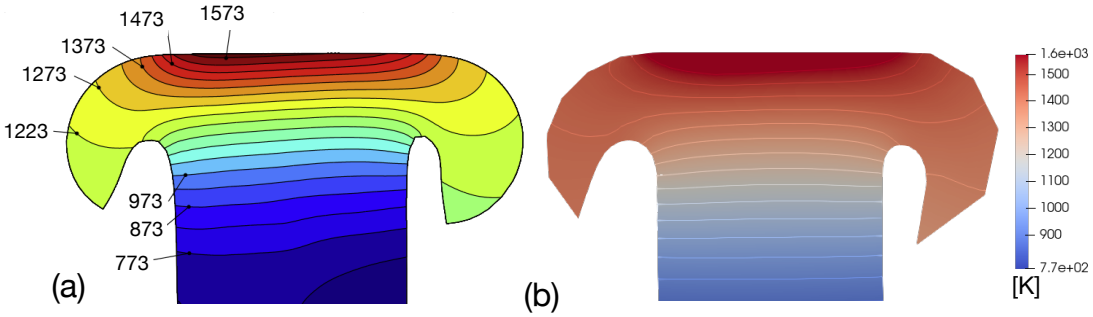

Figure 12: Comparison of the deformed shape at the end of the weld with the temperature distribution superimposed from (a) [26] and (b) the ALE formulation.

A fully Lagrangian simulation of the weld is now performed to assess its performance. Severe mesh distortion occurs around the weld interface, causing caused large deviations from the experimentally observed results, followed by failure in convergence of the solution steps. Figure 13 shows a comparison between the Lagrangian and ALE simulations at different stages of the weld. Early in the process, the differences between the Lagrangian and ALE simulations are small. As the mesh distortion in the Lagrangian simulation increases, however, the results deviate considerably. Since the ALE results correlate well with the experimental and numerical results from [26], this deviation confirms that excessive distortions limit the reliability of a fully Lagrangian formulation in simulation of friction welding processes, and shows the ALE formulation is effective in addressing this limitation.

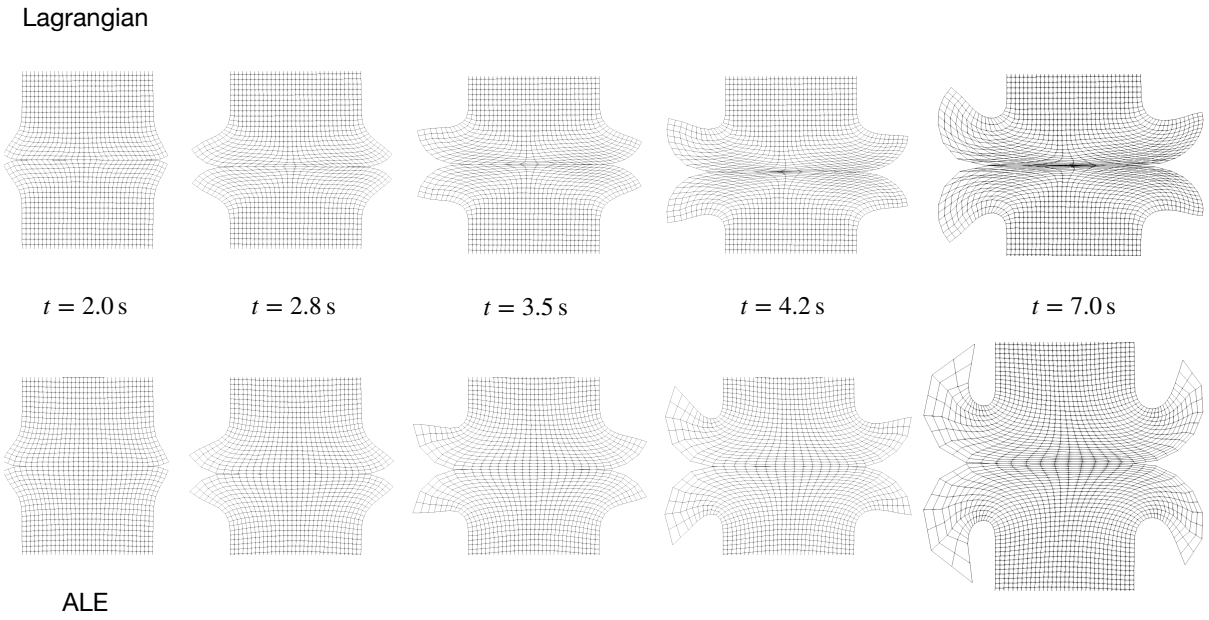

Figure 13: Comparison of the Lagrangian and ALE formulations at various point during the friction welding process.

6 Conclusions

This work has described the development and implementation of a large-deformation thermo-elastoviscoplasticity solver with thermomechanical friction contact, a key application being the numerical simulation of friction welding processes. A novel Arbitrary Lagrangian-Eulerian

(ALE) has been developed, validated with benchmark problems, used to simulate a friction welding process.

The novelty of the developed ALE formulation lies in that the deformation gradient between the current and material configurations is not required; the motion of the material configuration is represented only incrementally in terms of the reference velocity.

The ALE formulation presented and used improves on the state of the art of ALE approaches for finite strain plasticity, in that there is no need to keep track of the material configuration mesh, thus enabling simulation of more severe deformations. Furthermore, it is not necessary to use a Godunov-like technique for convection of the left Cauchy-Green deformation tensor, the equivalent plastic strain, and the deformation Jacobian. Rather, these are evaluated directly at the quadrature point positions before the incremental mesh motion. This alleviates convection accuracy considerations when choosing the mesh motion step size. This also makes it possible to use the developed remapping procedure unchanged for adaptive mesh refinement and coarsening, or for remeshing.

The implemented solver makes use of the rotational symmetry in rotary friction welding processes, with the reference motion decomposed into an in-plane component and a circumferential component. The in-plane component is updated in a split-step approach, and the circumferential component simultaneously with the deformation field.

The formulation and algorithms implemented in this work can be extended in a number of ways in order to simulate a broader range of friction welding and general metal- working processes. First, the rotational symmetry assumed in this work would have to be generalized to a fully three-dimensional implementation to accommodate friction stir welding and linear friction welding simulations. Another possible extension pertains to modelling, implementation and validation of self-contact, which is also relevant in some rotational friction welding applications.

The prediction of solid bonding in numerical simulation of friction welding processes remains an open problem [6]. The model developed in this work serves as a basis for modelling solid bonding, and predicting the transitional behaviour at the welding interface from contact between two bodies to deformation of one bonded body.

Acknowledgements

The work reported in this article has been carried out with the support of the National Research Foundation through the South African Research Chair in Computational Mechanics.

References

[1] C. Agelet de Saracibar. Numerical analysis of coupled thermomechanical frictional contact problems. computational model and applications. *Archives of Computational Methods in Engineering*, 5(3):243–301, 1998.

[2] J. Argyris and J. S. Doltsinis. On the large strain inelastic analysis in natural formulation part I: Quasistatic problems. *Computer Methods in Applied Mechanics and Engineering*, 20(2):213–251, 1979.

[3] F. Armero and E. Love. An arbitrary Lagrangian–Eulerian finite element method for finite strain plasticity. *International Journal for Numerical Methods in Engineering*, 57(4):471–508, 2003.

[4] W. Bangerth, R. Hartmann, and G. Kanschat. deal.II – a general purpose object oriented finite element library. *ACM Transactions on Mathematical Software*, 33(4):24/1–24/27, 2007.

[5] G. Bendzsak, T. North, and Z. Li. Numerical model for steady-state flow in friction welding. *Acta Materialia*, 45(4):1735–1745, 1997.

[6] G. Buffa and L. Fratini. Strategies for numerical simulation of linear friction welding of metals: a review. *Production Engineering*, 11(3):221–235, 2017.

[7] J. Chung and G. M. Hulbert. A time integration algorithm for structural dynamics with improved numerical dissipation: the generalized-α method. *Journal of Applied Mechanics*, 60(2):371–375, 1993.

[8] B. Crossland. Friction welding. *Contemporary Physics*, 12(6):559–574, 1971.

[9] Ø. Frigaard, Ø. Grong, and O. T. Midling. A process model for friction stir welding of age hardening aluminum alloys. *Metallurgical and Materials Transactions A*, 32(5):1189–1200, 2001.

[10] L. Fu, L. Duan, and S. Du. Numerical simulation of inertia friction welding process by finite element method. *Welding Journal*, 82(3):65S–70S, 2003.

[11] M. Grujicic, G. Arakere, B. Pandurangan, J. M. Ochterbeck, C. F. Yen, B. A. Cheeseman, A. P. Reynolds, and M. A. Sutton. Computational analysis of material flow during friction stir welding of AA5059 aluminum alloys. *Journal of Materials Engineering and Performance*, 21(9):1824–1840, 2011.

[12] X. He, F. Gu, and A. Ball. A review of numerical analysis of friction stir welding. *Progress in Materials Science*, 65(3):1–66, 2014.

[13] G. Johnson and W. Cook. A constitutive model and data for metals subjected to large strains, high strain rates and high temperatures. In *Proceedings of the Seventh International Symposium on Ballistics*, The Hague, The Netherlands, 1983.

[14] J. Lacy, S. Novascone, W. Richins, and T. Larson. A method for selecting software for dynamic event analysis: II—the Taylor anvil and dynamic Brazilian tests. In *Proceedings of the 16th International Conference on Nuclear Engineering*, volume 48175, pages 261–270, 2008.

[15] R. Landell, L. F. Kanan, D. Buzzatti, B. Vicharapu, A. De, and T. Clarke. Material flow during friction hydro-pillar processing. *Science and Technology of Welding and Joining*, 25 (3):228–234, 2020.

[16] T. Laursen and J. Simo. A continuum-based finite element formulation for the implicit solution of multibody, large deformation-frictional contact problems. *International Journal for Numerical Methods in Engineering*, 36(20):3451–3485, 1993.

[17] T. Lehmann and U. Blix. On the coupled thermo-mechanical process in the necking problem. *International Journal of Plasticity*, 1(2):175–188, 1985.

[18] W. Li, S. Shi, F. Wang, Z. Zhang, T. Ma, and J. Li. Numerical simulation of friction

welding processes based on ABAQUS environment. *Journal of Engineering Science and Technology Review*, 5(3):10–19, 2012.

[19] W. Li, F. Wang, S. Shi, and T. Ma. Numerical simulation of linear friction welding based on ABAQUS environment: Challenges and perspectives. *Journal of Materials Engineering and Performance*, 23(2):384–390, 2014.

[20] M. Maalekian. Friction welding–critical assessment of literature. *Science and Technology of Welding and Joining*, 12(8):738–759, 2007.

[21] R. R. Maurya and J. J. Kauzlarich. Reciprocating friction bonding apparatus, 1969. US Patent 3,420,428.

[22] A. Moal and E. Massoni. Finite element simulation of the inertia welding of two similar parts. *Engineering Computations*, 12(6):497–512, 1995.

[23] A. Needleman. A numerical study of necking in circular cylindrical bar. *Journal of the Mechanics and Physics of Solids*, 20(2):111–127, 1972.

[24] D. M. Neto and P. Neto. Numerical modeling of friction stir welding process: a literature review. *The International Journal of Advanced Manufacturing Technology*, 65(1–4):115–126, 2013.

[25] A. Rodríguez-Ferran, A. Pérez-Foguet, and A. Huerta. Arbitrary Lagrangian–Eulerian (ALE) formulation for hyperelastoplasticity. *International Journal for Numerical Methods in Engineering*, 53(8):1831–1851, 2002.

[26] D. Schmicker, K. Naumenko, and J. Strackeljan. A robust simulation of direct drive friction welding with a modified carreau fluid constitutive model. *Computer Methods in Applied Mechanics and Engineering*, 265(1):186–194, 2013.

[27] H. Schmidt and J. Hattel. A local model for the thermomechanical conditions in friction stir welding. *Modelling and Simulation in Materials Science and Engineering*, 13(1):77–93, 2005.

[28] J. Simo and T. Laursen. An augmented Lagrangian treatment of contact problems involving friction. *Computers & Structures*, 42(1):97–116, 1992.

[29] J. Simo and C. Miehe. Associative coupled thermoplasticity at finite strains: Formulation, numerical analysis and implementation. *Computer Methods in Applied Mechanics and Engineering*, 98(1):41–104, 1992.

[30] J. C. Simo and T. A. Laursen. An augmented Lagrangian treatment of contact problems involving friction. *Computers & Structures*, 42(1):97–116, 1992.

[31] G. I. Taylor. The use of flat-ended projectiles for determining dynamic yield stress I. theoretical considerations. *Proceedings of the Royal Society of London. Series A. Mathematical and Physical Sciences*, 194(1038):289–299, 1948.

[32] W. Thomas, E. Nicholas, J. Needham, M. Murch, P. Temple-Smith, and C. Dawes. Friction stir welding, international patent application, 1991. GB Patent Application PCT/GB92/02203.

[33] A. Vairis and M. Frost. Modelling the linear friction welding of titanium blocks. *Materials Science and Engineering: A*, 292(1):8–17, 2000.

[34] D. Veljic, M. Rakin, M. Perovic, B. Medjo, Z. Radakovic, P. Todorovic, and M. Pavisic. Heat generation during plunge stage in friction stir welding. *Thermal Science*, 17(2):489–496, 2013.

[35] V. I. Vill. *Friction Welding of Metals*, volume 1. American Welding Society; Trade Distributor: Reinhold Pub. Co., 1962.

[36] P. Wriggers, C. Miehe, M. Kleiber, and J. Simo. On the coupled thermomechanical treatment of necking problems via finite element methods. *International Journal for Numerical Methods in Engineering*, 33(4):869–883, 1992.

[37] Y. Xu, H. Jing, Y. Han, and L. Xu. Numerical simulation of the effects of various stud and hole configurations on friction hydro-pillar processing. *International Journal of Mechanical Sciences*, 90:44–52, 2015.

[38] Q. Zhang, L. Zhang, W. Liu, X. Zhang, W. Zhu, and S. Qu. 3D rigid viscoplastic fe modelling of continuous drive friction welding process. *Science and Technology of Welding and Joining*, 11(6):737–743, 2006.